Compact Electromagnetic Band-Gap Structures (EBG) and Its Applications in Antenna Systems

by

Jingkun Zeng

A thesis
presented to the University of Waterloo
in fulfilment of the
thesis requirement for the degree of
Master of Applied Science
in
Electrical and Computer Engineering

Waterloo, Ontario, Canada, 2013

Author’s Declaration

I hereby declare that I am the sole author of this thesis. This is a true copy of the thesis, including any required final revisions, as accepted by my examiners.

I understand that my thesis may be made electronically available to the public.

Abstract

This dissertation is focused on design of compact electromagnetic magnetic band-gap structures (EBG). Several popular compact techniques are introduced and analyzed with equivalent surface impedance model. A novel compact EBG structure is investigated. Compared to the conventional uniplanar compact photonic band gap (UC-PBG) structure, a size reduction of 64.7% is achieved. A distinctive band gap is observed at 2.45 GHz with around 100 MHz bandwidth and zero reflection phase. Antenna applications of this novel EBG structure, including EBG patch antenna and EBG antenna array, have been presented. Simulations results further verify its characteristic of suppressing surface waves. For the EBG patch antenna, a more focused radiation pattern is obtained compared to a normal patch antenna. For an antenna array, the presence of EBG structure reduces the mutual coupling between the two radiating elements by 6 dB.

Acknowledgements

I would like to express my sincere appreciation to my supervisor, Prof. Safieddin Safavi-Naeini. During the entire course of my research work, his extensive knowledge and experience have always provided me with wisely guidance and strong support. It is certainly a great enjoyment in my life to work with such a talented professor who put completely trust and confidence in his students. It is because of his suggestion that I could start working on the electromagnetic band gap structures and finally accomplished this dissertation.

Special thanks go to our kindly group members who devoted their time and effort with fabrication issues of my research work. Thanks to Dr. Hassan Safdary, because of his help I could have a first glance of circuit fabrication. I should give extreme appreciation to Dr. Mehrbod Mohajer Jasebi, Rasoul Keshavarzi-Valdani and Dr. Aidin Taeb, who would like to spend a lot of valuable time and make every possible effort to deal with my design. I must also thank Jose (Roberto) Romero and Dr. Gholamreza Z. Rafi, who offered valuable help during the fabrication progress. Without all your devotion, it is impossible to have those precisely fabricated circuits.

Many thanks to Prof. Chandra Kudsia who gave me two impressive graduate courses. It is certainly amazing to be in his class which is not only reviewing the book material, but exploring profound meaning behind every formula and figure. The knowledge and scientific spirit I obtained from his teaching have offered me a firm foundation to my future research work. It was a pleasant to have another two graduate courses under the guidance of Prof. Raafat R. Mansour. In his cheerful class, I have gained special interest and in-depth knowledge about microwave filter design, which was proved to be extremely useful in practical research work. Also, I give sincere thanks to Prof. Bosco Leung. It was unforgettable that he pointed out my mistake in the course project and how patiently he was explaining it to me during his office hour.

There is no doubt that I have shared a great time with my fellow researchers, Saman Jafarlou, Alireza Zandieh, Yushi Hu, Xin Fu, Joyce Li, Qin Li, Maofeng Yang. Our discussions around class and office have enriched my thoughts and widened my scope, getting me to know more about other research areas.

This research was supported by National Science and Engineering Research Council (NSERC) of Canada, and Research In Motion (RIM). Many thanks to these organizations for their devotion to our research work.

At last, I would like to appreciate my parents. Although, they are thousands of miles away from where I live, their trust, understanding and respect to my decisions have always been great support to my study in Waterloo.

Table of Contents

List of Figures

List of Tables

Chapter 1

Introduction

High-impedance Electromagnetic Band-Gap structures (EBG) are typically periodic artificial media, which exhibit properties of preventing electromagnetic wave propagation in specified directions and frequency ranges. An initial research on EBG structure at microwave frequencies was conducted by Prof. E. Yablanovitch and his research group in [1], which explained many of its properties (surface current suppression and zero reflection phase) using an effective surface impedance model. Since then, theory and practical applications of EBG structure has become an extensive research area due to its unusual properties and design flexibilities. Consequently, numerous of EBG structures have been successfully employed to realize novel high performance devices such as filters, waveguides, antennas, etc. [2], [3], [4].

One important issue in EBG structure research is designing miniaturized structures integrated with miniaturized antennas to achieve ultra-compact systems at a relatively low frequency band (1-10 GHz). Conventional antenna miniaturization methods such as dielectric loading [5], meandering [6] and shorting pings [7] usually cause narrow bandwidth, undesired radiation pattern and low radiation efficiency [8]. Thus, strong interest exists in employing EBG structures to enhance antenna performance. Generally speaking, antennas can benefit from EBG structures in two ways. On one hand, EBG structure is utilized as high impedance ground planes to suppress undesired surface waves and mutual couplings. This leads to an enhancement in maximum gain, smooth pattern, side/back lobes reduction, etc. On the other hand, EBG structure provides in-phase image currents with respect to currents in antennas. This allows low-profile antenna realizations that are impossible on ordinary ground planes [9].

Due to these advantages, many publications are focused on compact EBG structure and EBG antenna systems. In [10], a popular uniplanar compact EBG structure (UC-PBG) is proposed. Compared to traditional designs, vias and multilayer substrates are not required. Further enhancement in compactness based on this UC-PBG using vias, mitering lines, meandered loops, inter-digital capacitors have been introduced in [11], [12]. Low profile wire antennas with EBG ground are studied in [13], [14], [15]. In [16] and [17], EBG

structure is employed to on-body antennas to reduce sensitive absorption rate (SAR). Other applications of EBG structures such as Multi-band antenna, LTCC and bandwidth enhancement are introduced in [18], [19] and [20], respectively.

Another area of EBG structure research is focused on characteristics of its unique properties, providing simple and fast design approaches. [21] presents a study on in-phase reflection and wave suppression characteristics of EBG structure. In [22], a method of designing controlled bandwidth EBG structure is demonstrated. Spectral domain method is explained in [23] to prove that capacitive surfaces can perform as perfect magnetic conductors in a relative low frequency range.

In this research, a novel compact EBG structure is proposed. The design starts with analysis of equivalent lumped circuit model for the EBG unit cell. Then the circuit model is tuned in a circuit simulator using distributed elements in the simulator's library. Later, accurate design modeling is carried out by a FEM simulator to meet specified design requirements such as resonant frequency, bandwidth, in-phase reflections, dispersion property, etc..

This dissertation is composed of four chapters. Chapter 2 first describes the effective surface impedance model of EBG structures. In the limit where the wavelength is much longer than the period of the surface texture, the EBG model can be simplified to equivalent lumped elements: inductors and capacitors, and its properties can be summarized into its surface impedance. Periodic structures are analyzed, followed by an example of equivalent circuit for EBG structure unit cell. Section 2.2 introduces several popular compact EBG structures. Compact designs using edge-located via, slot-strip configuration, inter-digital capacitor and Hilbert-curve are discussed. In Section 2.3, a novel compact high-impedance EBG structure is proposed based on the Mushroom-like EBG structure. Configuration and equivalent circuit model for a single unit cell are established. The circuit model is then proved in Advanced Design System (ADS) circuit simulator. Section 2.3.3 to Section 2.3.6 is dedicated to employing FEM simulator (Ansoft HFSS) in the design process. Simulation results of reflection phase and dispersion diagram of the proposed EBG structure is illustrated, as well as the parameter study. Finite-element models with microstrip lines are analyzed in Section 2.3.7.

Chapter 3 is mainly concerned with integrating the compact EBG structure proposed in Chapter 2 with patch antennas. It starts with basic analysis of current source near an infinite

plane with arbitrary reflection phase in Section 3.1. The influence of reflection phase on current source radiation power is discussed and the need for EBG plane is obvious. Section 3.2 gives a special case of high-impedance EBG ground combining with a patch antenna followed by FEM (Ansoft HFSS) simulation. The result clearly shows that surface waves on the ground are significantly suppressed. This conclusion is further proved in Section 3.3 when the proposed EBG structure is integrated to an antenna array.

At last, Chapter 4 concludes this research and addresses possible future work. A brief introduction is given on the application to Body Area Network (BAN).

Chapter 2

Compact EBG Design

In Appendix A, the properties of surface waves on different types of interfaces are discussed. For the case of impedance surface, TM surface waves can only propagate on an inductive surface. While TE surface waves are only supported by a capacitive surface. Thus, to eliminate propagation of both TM and TE surface waves, it seems necessary to design a special surface structure which simultaneously possesses inductive and capacitive surface impedance. This could be thought of as a LC resonant structure. In fact, surface waves can be prevented over a finite frequency band by texturing periodic lumped-element resonance structures on the surface. As the surface waves scatter from the discontinuity, the radiation interference prohibits them from propagating, producing a high-impedance band-gap over certain frequency ranges. Earlier EBG structure working at radio/microwave frequencies can be traced to the structure known as photonic band-gap material [24]. Since then, extensive studies have been conducted in applying EBG structure to RF/microwave communications [25], [26].

To help analyzing the EBG structure, effective surface impedance models are used to describe its properties [1]. Effective surface impedance models usually consist of lumped inductors and capacitors, presenting high-impedance property in certain frequency ranges. The EBG surface is assigned a surface impedance equals to the equivalent impedance of a resonant LC circuit. This method is valid as long as the period of the textured structure is much smaller compared to the wave length of surface waves.

In this chapter, properties of an infinite periodic structure are analyzed and an example of LC circuit that can serve as effective surface impedance models is discussed [12]. Then, some previous samples of compact EBG structures are given. In Section 2.3, a novel compact EBG structure for planar microwave circuits is proposed. As compare to structures based on mushroom-like structures, via holes are not required in this proposed structure, which makes it simple to be fabricated. A distinctive bad-gap centered at 2.45 GHz is observed.

2.1 Effective Surface Impedance Model

2.1.1 Analysis of Periodic Structures

The transmission property of a two-port network can be described in terms of its ABCD matrix [27], as shown in Figure 2-1 and (2.1.1).

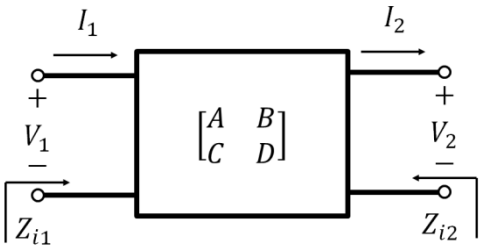

Figure 2-1 A two-port network described with ABCD matrix.

$$V_1 = AV_2 + BI_2 \tag{2.1.1a}$$

$$I_1 = CV_2 + DI_2 \tag{2.1.1b}$$

or in matrix form as,

$$\begin{bmatrix} A & B \\ C & D \end{bmatrix} \begin{bmatrix} V_2 \\ I_2 \end{bmatrix} = \begin{bmatrix} V_1 \\ I_1 \end{bmatrix}$$

The input impedance at port 1 and port 2 can be defined as

$$Z_{i1} = \frac{V_1}{I_1} \tag{2.1.2a}$$

$$Z_{i2} = -\frac{V_2}{I_2} \tag{2.1.2b}$$

Combine (2.1.1) and (2.1.2) together, we have

$$Z_{i1} = \frac{AV_2 + BI_2}{CV_2 + DI_2} = \frac{-AZ_{i2} + B}{-CZ_{i2} + D} \tag{2.1.3}$$

If the two port network is symmetric and the two ports are well matched, then

$$A = D \tag{2.1.4}$$

$$Z_{i1} = -Z_{i2} \tag{2.1.5}$$

Solving (2.1.3), (2.1.4) and (2.1.5) yields

$$Z_{i1} = \pm\sqrt{\frac{B}{C}} \tag{2.1.6}$$

Hence, (2.1.6) represents the characteristic impedance of this two port network. The $\pm$ solutions correspond to positively and negatively traveling waves, respectively.

From (2.1.1), transmission coefficient from port 1 to port 2 can also be defined.

$$T = \frac{V_2}{V_1} = \sqrt{\frac{D}{A}}(\sqrt{AD} - \sqrt{BC}) \tag{2.1.7}$$

For a symmetric network with $A = D$,

$$T = A - \sqrt{BC} \tag{2.1.8}$$

A periodic structure is obtained by cascading the two-port networks as unit cells. This is shown in Figure 2-2. Here, the coupling effect between the any two unit cells is ignored. In the same manner as in the previous section, transmission property of a single unit cell is described with its ABCD matrix.

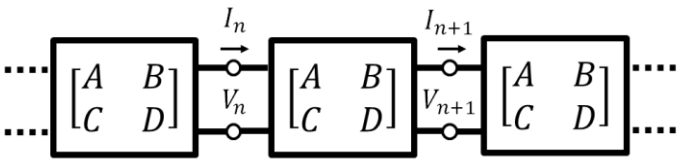

Figure 2-2 A cascade periodic network.

$$\begin{bmatrix} V_n \\ I_n \end{bmatrix} = \begin{bmatrix} A & B \\ C & D \end{bmatrix} \begin{bmatrix} V_{n+1} \\ I_{n+1} \end{bmatrix} \tag{2.1.9}$$

Now let us assuming that voltages and currents at the two ports of a unit cell have the relationship of

$$V_{n+1} = V_n T \tag{2.1.10a}$$

$$I_{n+1} = I_n T \tag{2.1.10b}$$

Solving (2.1.9) and (2.1.10), we have

$$\begin{bmatrix} A-T & B \\ C & D-T \end{bmatrix} \begin{bmatrix} V_{n+1} \\ I_{n+1} \end{bmatrix} = 0 \tag{2.1.11}$$

Taking symmetry of the unit cell into consideration, $A = D$, (2.1.11) can be simplified as,

$$A^2 + T^2 - 2AT - BC = 0$$

Then,

$$T = A \pm \sqrt{BC} \tag{2.1.12}$$

We can define characteristic impedance at the terminals of the nth unit cell as

$$Z_B = \frac{V_{n+1}}{I_{n+1}} \tag{2.1.13}$$

This impedance is also referred to as the Bloch impedance for periodic crystal lattices [28]. From (2.1.11) we have that

$$(A-T)V_{n+1} + BI_{n+1} = 0 \tag{2.1.14}$$

Inserting (2.1.13) into (2.1.14) yields

$$Z_B = -\frac{B}{A-T} \tag{2.1.15}$$

For symmetrical and reciprocal unit cells, (2.1.12) is employed to simplify (2.1.15) as

$$Z_B = \pm\frac{B}{\sqrt{BC}} = \pm\sqrt{\frac{B}{C}} \tag{2.1.16}$$

Compare (2.1.6), (2.1.8), (2.1.15) and (2.1.16), we found that an infinite periodic circuit can be fully described using one of its unit cell. Thus, effective surface impedance of an infinite periodic structure is equivalent to the characteristic impedance of a single unit cell.

2.1.2 Equivalent Circuits for a Single Unit Cell in Periodic Structures

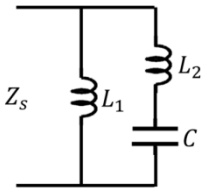

Figure 2-3 Inductive loaded series LC resonant circuit.

For the circuit in Figure 2-3, we have the surface impedance in the form below.

$$Z_s = \frac{j\omega L_1(1-\omega^2 L_2 C)}{1-\omega^2(L_1+L_2)C} \tag{2.1.17}$$

The equivalent surface impedance is plotted against frequency in Figure 2-4 and the corresponding dispersion diagram is shown in Figure 2-5. At low frequencies the surface impedance is inductive and supports TM waves. From the dispersion diagram we can see

that TM waves below the resonance stay close to the light line as they do on a metal-dielectric interface. As the frequency increasing, the TM curve begins to bend over. The slope of the curve indicates that as the frequency approaching resonance, TM waves are effectively slowed down by the surface.

The surface impedance is capacitive at intermediate frequencies and TE waves are supported. The TE curve in dispersion diagram bends away from the light line except for a small section near the resonance. Around the resonance, the surface impedance is very high and group velocities for both TM and TE waves are very low since the two dispersion curves bent away from the light line. Thus, we can consider the area between TM and TE curves in Figure 2-5 as a stop band for wave propagation. The lower limit is defined as the maximum point of the TM curve, and the upper limit is defined as the intersection between light line and the TE curve.

The surface impedance turns to inductive again at high frequencies, which means the surface supports TM waves at high frequencies.

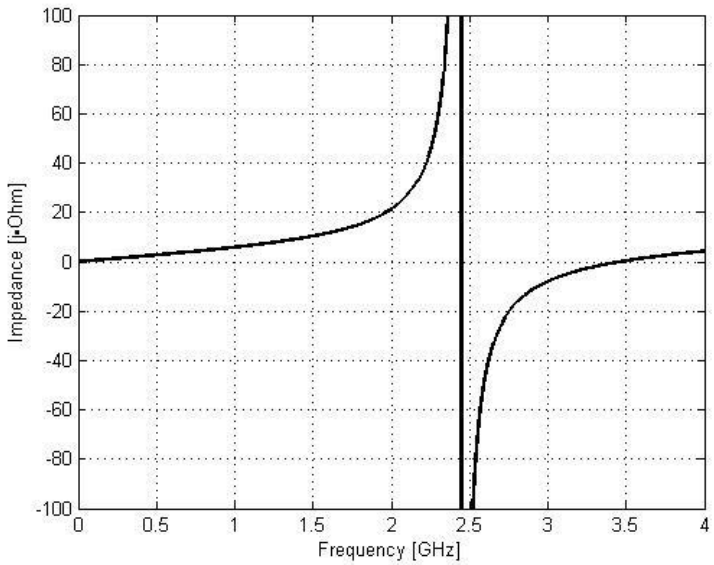

Figure 2-4 Impedance of an inductive loaded series LC resonant circuit.

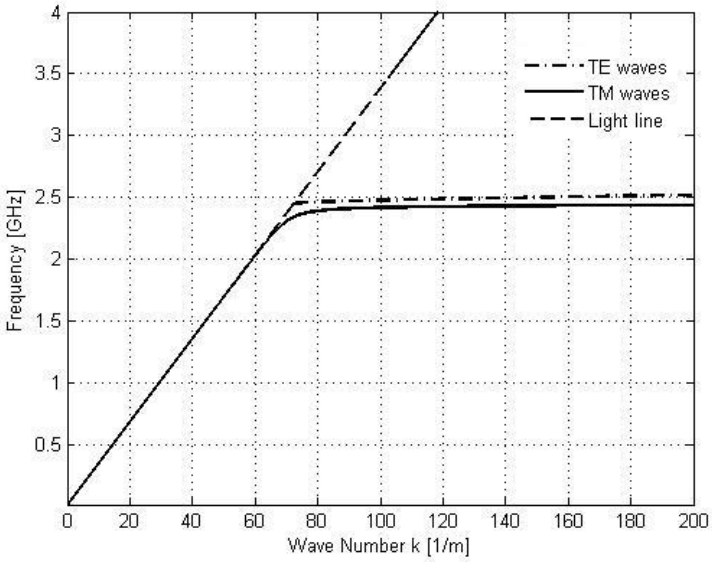

Figure 2-5 Dispersion diagram for an inductive loaded series LC resonant circuit.

2.2 Samples of Compact EBG Structure

The issue of compactness in designing EBG structure has attracted extreme attention in the research process. The miniaturising of element size allows EBG structures to be further employed to integrated RF/microwave circuits.

2.2.1 Edge-located Via

One simple modification to reduce the size of mushroom-like structure is to use edged-located vias, as shown in Figure 2-6. This method was first proposed in [29]. The purpose of moving the via position from the center to the edge is to increase the electrical path of each element shown in Figure 2-6. This edged-located configuration decreases resonant frequency of traditional mushroom-like structure by 20%.

The size can be further reduced by using the structure shown in Figure 2-7. The design of this compact structure is based on a miniaturized hairpin resonator [30]. By combining edged metallic vias connecting to the ground plane, a size reduction of approximately 40% is achieved. The resonator could be designed according to the resonance condition equation derived in [31].

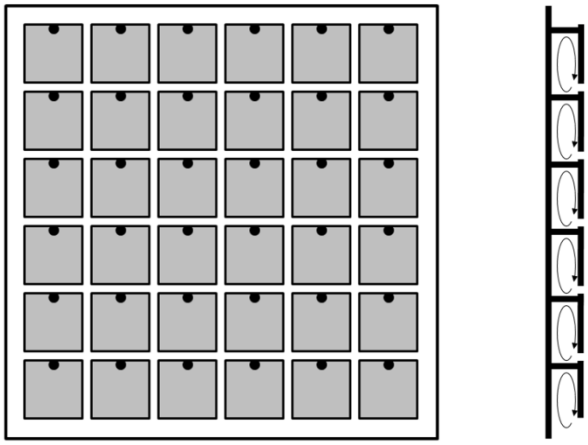

Figure 2-6 Mushroom-like EBG structure with edged-located vias.

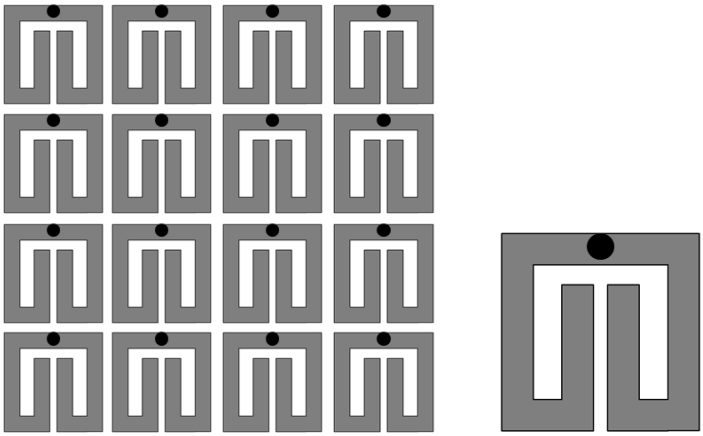

Figure 2-7 Hairpin resonator EBG structure.

2.2.2 UC-PBG Surface

The schematic of uniplaner compact photonic band-gap (UC-PBG) surface [32] is shown in Figure 2-8. The surface structure is a lattice of meta-material pads mounted on a substrate. Each unit cell of the lattice consists of a square metal pad with four connecting branches. Notice that capacitance is introduced by the gaps between neighboring pads and inductance is provided by the narrow branches. The series inductors combined with the shunt capacitors constitute an array of parallel LC circuits, which has high surface impedance at resonant frequency.

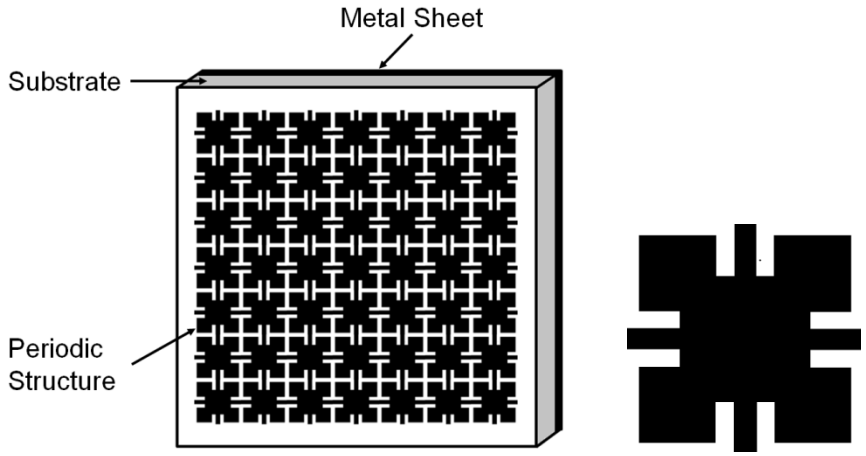

Figure 2-8 UC-PBC surface structure.

Compared to mushroom-like structure, UC-PBG has a more compact size and less complex configuration (no via). These properties make it easy to be integrated with other radio frequency and microwave components. Because of relatively broader bandwidth and the surface wave suppression effect, UC-PBG structure has been employed to numerous applications, such as compact antennas, mutual coupling reduction, filter applications, leakage suppression, and harmonic tuning for power amplifiers [33].

2.2.3 Slot-strip EBG Structure

The schematic of slot-strip EBG structure is shown in Figure 2-9(a), which is also known as folk-like structure [34]. Compared to the mushroom-like structure, this design has a more compact configuration. Each element of this EBG structure lattice has a slot etched on one edge of the metal patch and a stretched strip connecting to the opposite edge.

These slots and strips provide additional gap length between the neighboring patches, leading to significant increase in capacitance of the equivalent LC circuit. Thus, resonant frequencies of LC circuits are reduced. The area occupied by each patch of the fork-like structure is reduced more than 40% compared to the mushroom-like structure. Another slot-strip EBG structure mentioned in [34] is shown in Figure 2-9(b). Every four F-like patches comprise an isotropic configuration and a 41.6% size reduction is achieved compared to the mushroom-like structure.

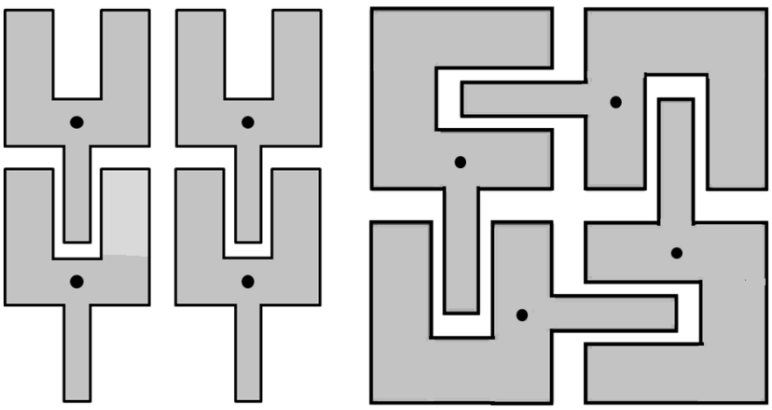

(a) (b)

Figure 2-9 (a) Folk-like and (b) F-like EBG structure.

2.2.4 Inter-digital Structure

Inter-digital capacitor was first introduced to enlarge the effective capacitance in microwave integrated circuits in [35]. It has been employed as a common technique to design compact EBG structure.

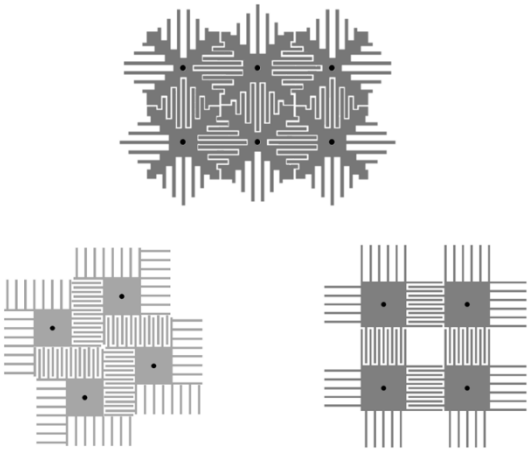

Figure 2-10 Examples of inter-digital EBG structure.

Figure 2-10 shows three inter-digital EBG structure. The branches of each elements cross over with the neighboring one, leading to a larger fringe capacitor compared to the conventional mushroom-like structure. Thus, very compact EBG structure can be obtained at lower frequencies [36], [37], [38]. Method to calculate the value of an inter-digital capacitor is explicitly introduced in [39].

2.2.5 Hilbert Curve Structure

A Hilbert-curve usually has the property of long electrical length but occupies a compact area. As the iteration order increasing, a Hilbert curve can maintain its size while enlarging its length. Moreover, this space-filling geometry is a planer structure, which allows it to be easily fabricated. The Hilbert curve geometry has been employed to design small antennas [40], [41], [42], as well as frequency selective surface (FSS) [43].

A Hilbert-curve EBG structure can be designed by creating a periodic array of Hilbert elements over a PEC ground plane as is shown in Figure 2-12. The band-gap is primarily determined by the order number of the Hilbert Curve elements, i.e., the length of the curve [44].

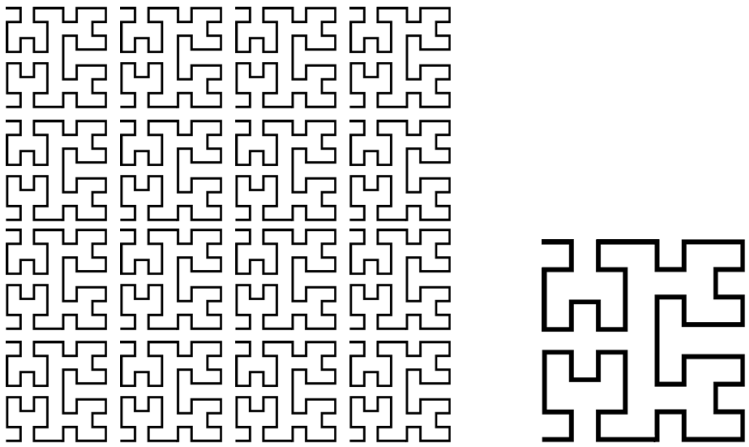

Figure 2-12 Hilbert-curve high-impedance surface structure.

2.3 A Novel Compact EBG Structure

The novel compact EBG structure proposed in this section is based on the Mushroom-like EBG structure that first introduced in [1]. Instead of using a 3-dimension configuration, the newly proposed EBG structure is folded in a 2-dimension planar. Thus, conducting vias are not needed. Also, microstrip inter-digital capacitors are introduced to enhance the compactness of this design.

2.3.1 Mushroom-like Structure

An example of top view and side view of Mushroom-like structure is shown in Figure 2-13. The unit cell of mushroom-like structure is comprised of square metal patches raised above a flat metal ground plane. These square metal patches are connected to the flat metal ground plane by vertical conducting thin posts from their centers, which are represented as dots in Figure 2-13.

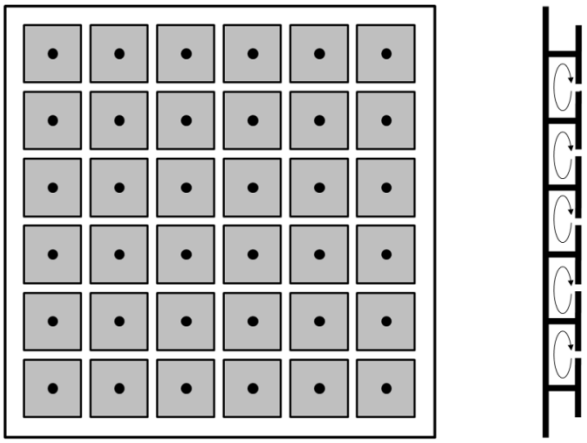

Figure 2-13 Mushroom-like EBG structure.

A propagating surface wave will introduce currents and cause charges accumulated at the edge of patches. Thus, capacitance is introduced. The inductance is provided by the thin conducting posts that connecting the patches and the ground plane.

2.3.2 Design of Novel Compact EBG Structure

Schematic of the compact EBG structure is shown in Figure 2-14. In top view, the periodic metal layer consists of inter-digital capacitors and inductive strips, forming a distributed LC network. The EBG structure has a two-layer structure with different dielectric constants, as shown in Figure 2-14(b). The top layer is used for supporting antennas. The bottom layer separates the periodic metal surface and a flat metallic surface. The top substrate used is RO 3010 with a relatively high dielectric constant of 10.2, compared to the bottom substrate RO 3003 with a dielectric constant of 3. Thus, more power will scatter to the top side when an EBG structure surface is illuminated by an antenna, leading to higher radiation efficiency of the entire system.

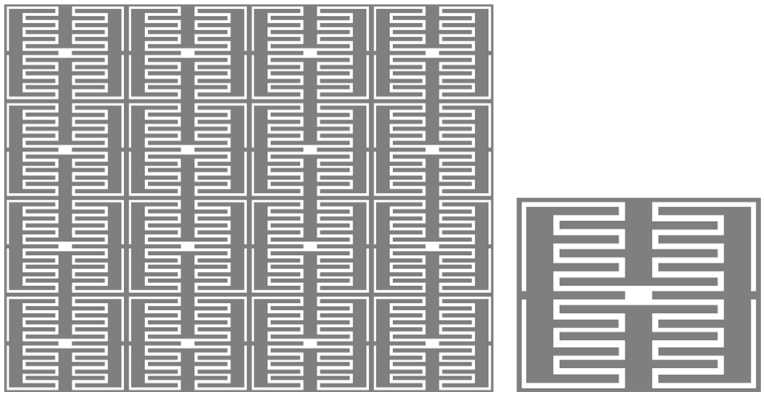

(a)

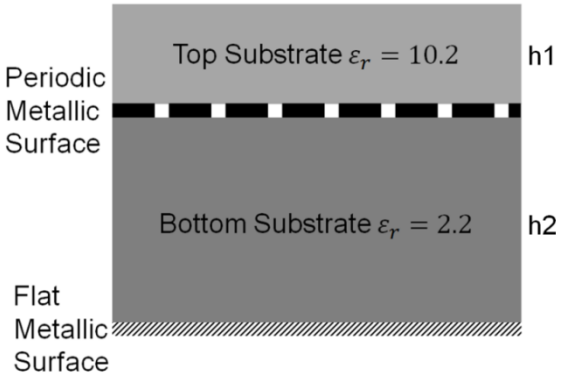

(b)

Figure 2-14 (a) Top view and (b) cross section of the proposed compact EBG structure.

The proposed EBG structure is designed at 2.45 GHz. Dimensions of a unit cell are illustrated in Figure 2-15 and Table 2-1. Each unit cell consists of four LC resonant circuits. The capacitance is provided by the inter-digital capacitor and the inductance is originated from the narrow strip. Since the period (largest side of a unit cell $= 0.073\lambda_{2.45GHz}$) of the proposed EBG structure is much smaller than the wavelength at resonance, its electromagnetic behavior can be explained using a simple LC circuit model.

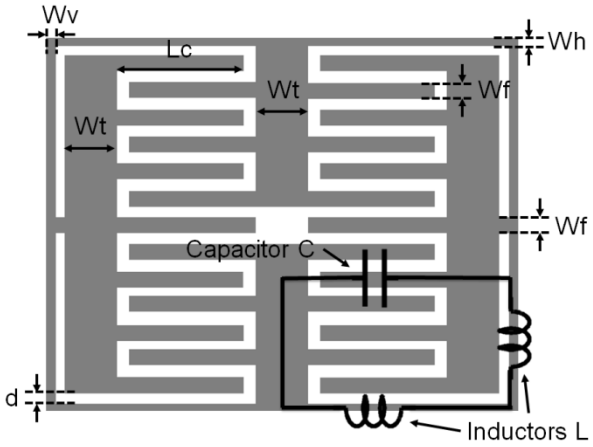

Figure 2-15 Details and equivalent circuit of a unit cell.

Table 2-1 Dimensions of a unit cell

Parameter	Dimension [mm]	Parameter	Dimension [mm]
W_h	0.15	L_c	2.4
W_v	0.15	h_1	1.27
W_t	1	h_2	3.175
W_f	0.3	d	0.2

According to the discussion in Section 2.1, we can assign surface impedance to the periodic structure equal to the equivalent impedance of a single LC circuit. The equivalent surface impedance, resonant frequency and bandwidth are given by the following expressions.

$$Z_s = \frac{j\omega L(1-\omega^2 LC)}{1-2\omega^2 LC} \tag{2.3.1}$$

$$\omega_0 = \frac{1}{\sqrt{2LC}} \tag{2.3.2}$$

$$BW \propto \sqrt{\frac{L}{C}} \tag{2.3.3}$$

The surface impedance is inductive at low frequencies and thus supports TM surface waves. Then it turns to capacitive at intermediate frequencies and supports TE surface waves. At high frequencies, it turns back to inductive and support TM surface waves again. Around the first pole of $1/\sqrt{2LC}$, the impedance becomes very high. Thus, the surface suppresses propagation of both TM and TE surface waves and radiates efficiently. Also, it reflects external electromagnetic waves with a zero reflection phase and behaves as a magnetic conductor.

Transmission properties of a single LC circuit can be quickly illustrated using Advanced Design System (ADS) circuit simulator, as shown in Figure 2.16. All the feature sizes in Table 2-1 are available for the library components. The simulation result plotted in Figure 2-17 accurately predicts the position of resonance.

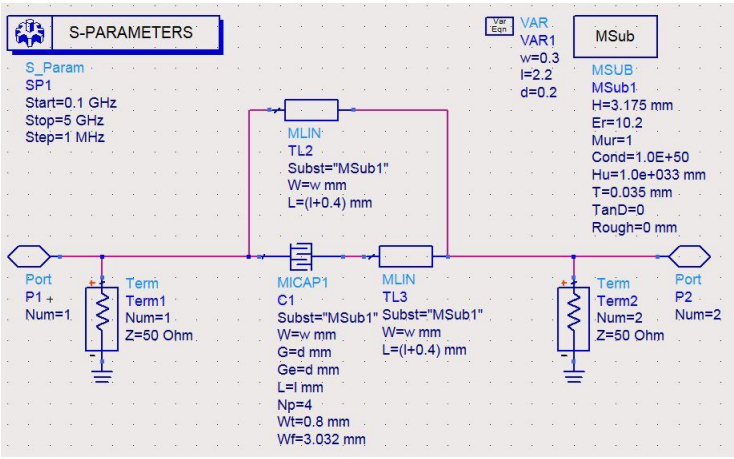

Figure 2-16 Schematic of a resonant element in ADS.

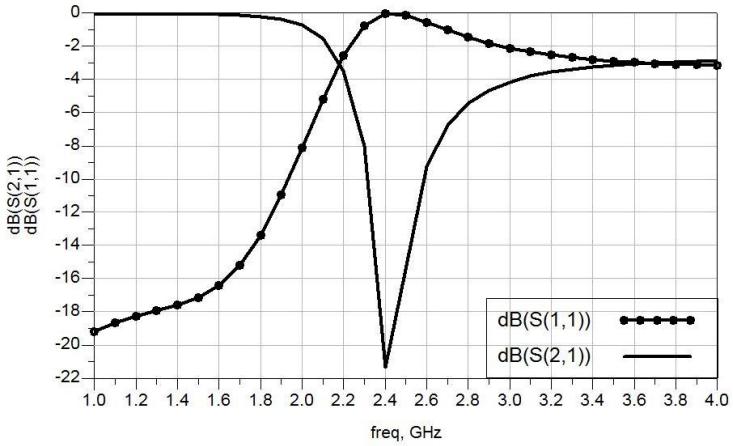

Figure 2-17 S-parameters of a resonant element.

To achieve lower resonant frequencies, the LC circuits in each unit cell can either load larger inductors or capacitors. However, a larger capacitance leads to reduction of bandwidth, as a direct result from (2.3.3).

2.3.3 HFSS Periodic Boundary Conditions

Periodic boundary conditions in HFSS allow users to simulate infinite periodic plane within the model of a single unit cell. It is based on defining two types of surfaces: master and slave. The electric field on a slave boundary matches the electric field on its corresponding master boundary within a phase difference [45] such that,

$$E_{slave} = e^{j\psi} E_{master}$$

$$\psi = \frac{2\pi d}{\lambda} sin\theta cos\phi$$

where d is the normal distance between the master and slave boundaries. θ and ϕ are spherical co-ordinates angles indicating the direction of incident wave.

To evaluate electromagnetic properties of the proposed EBG structure, a unit cell model with periodic boundary conditions on four sides is constructed in HFSS, as shown in Figure 2-18. Since the surface structure is open to air, an air box with height of approximately six times of the EBG structure thickness is defined above.

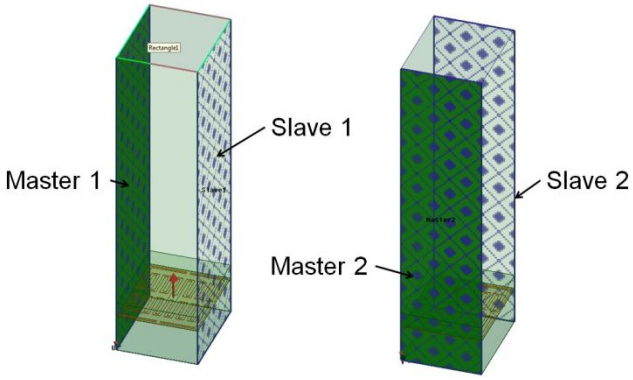

Figure 2-18 Unit cell model with periodic boundary conditions on four sides.

By applying different boundary conditions on top of the vacuum box, this model can be used to simulate either reflection phase or dispersion diagram, which will be discussed in the next two sections.

2.3.4 Reflection Phase

Now consider a standing wave formed by incident waves and reflected waves on a general impedance surface, as shown in Figure 2-19. Equivalent circuit for this model is shown in Figure 2-20.

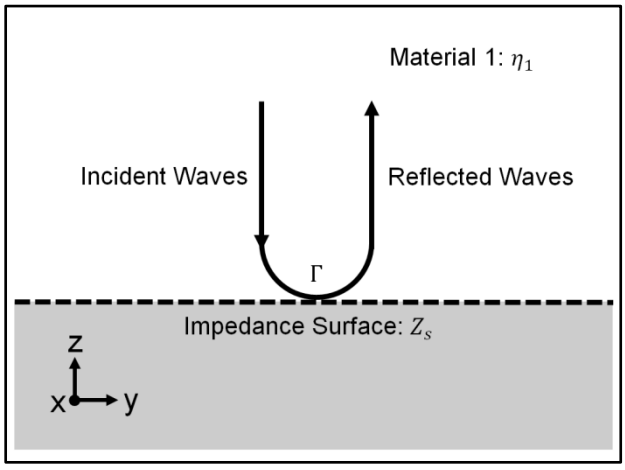

Figure 2-19 A standing wave on a general impedance surface.

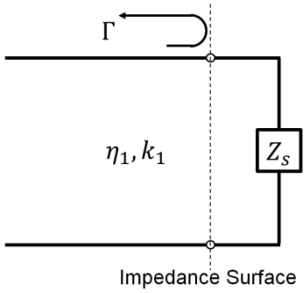

Figure 2-20 Equivalent circuit for a standing wave on a general impedance surface.

According to transmission line theory [27], the reflection coefficient at the surface is determined by the surface impedance Z_s and intrinsic impedance of material 1 η_1 in the form below,

$$\Gamma = \frac{Z_s - \eta_1}{Z_s + \eta_1} = |\Gamma| e^{j\Delta\theta} \tag{2.3.4}$$

$\Delta\theta$ is the phase difference between the incident and reflected waves at the surface.

$$\Delta\theta = Im\{\ln \Gamma\} = Im\left\{\ln \frac{Z_s - \eta_1}{Z_s + \eta_1}\right\} \tag{2.3.5}$$

When the surface impedance Z_s is much smaller than the intrinsic impedance of material 1, the reflection coefficient is -1 and the reflection phase is $\pm\pi$. This means that the wave has a short circuit at the surface, such as in the case of metal-dielectric interface. On the other hand, if the surface impedance is much larger than the intrinsic impedance, the reflection coefficient is 1 and the reflection phase tends to be zero, which indicates that the wave has an open circuit when impinging on the surface. Substitute Z_s in (2.3.5) with results in (2.3.1), we can plot the reflection phase against frequency for the case discussed in Section 2.1.2. As shown in Figure 2-21, the reflection phase of each case goes through zero when the surface presents high impedance property.

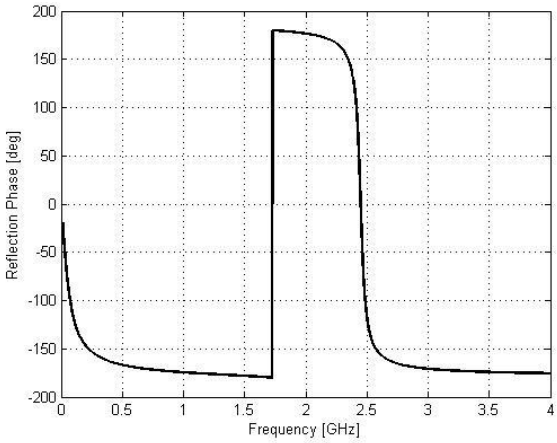

Figure 2-21 Reflection Phase of inductive loaded series LC resonant circuit.

To see the reflection phase of the proposed EBG structure, we apply driven mode in HFSS to solve the model introduced in Section 2.3.3. In addition to the periodic boundary conditions, a Floquet port is assigned at the top boundary to generate incident waves normally illuminate the surface and receive reflected waves, as shown in Figure 2-22.

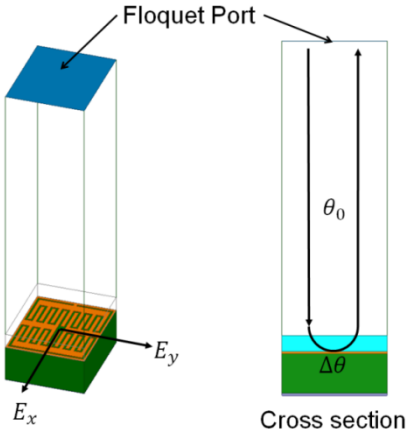

Figure 2-22 Unit cell model with a Floquet port on top boundary.

Here θ_0 represents the phase change when the incident wave propagates from the port to the surface. $\Delta\theta$ represents the reflection phase at the surface. The phase of reflection coefficient at the port can be expressed as,

$$\theta_\Gamma = 2\theta_0 + \Delta\theta \tag{2.3.6}$$

To determine the reflection phase $\Delta\theta$, a PEC surface is used as a reference. This can be simply done by replacing the EBG structure with a perfect conductor surface, which is known to have a reflection phase of π. In the same manner, the phase of reflection coefficient at the port is computed as,

$$\theta_{\Gamma_{PEC}} = 2\theta_0 + \pi \tag{2.3.7}$$

Using the two equations above, $\Delta\theta$ can be calculated as,

$$\Delta\theta = \theta_\Gamma - \theta_{\Gamma_{PEC}} + \pi \tag{2.3.8}$$

The phase of reflection coefficients for both EBG structure and PEC models can be extracted from HFSS simulation results and calculated using (2.3.8).

For most of the cases, the proposed EBG structure has different resonant frequencies when incident waves are polarized in different directions, shown as E_x and E_y in Figure 2-22. This can be solved by tuning size parameters of the unit cell. Thus, resonant frequencies for both polarized direction can be adjusted to the same frequency range.

The final result is plotted with Matlab, as shown in Figure 2-23. At very low and very high frequencies, the reflection phase is ±180 deg, and the EBG structure behaves like PEC. The reflection phase downward and crosses through zero at the resonant frequency. The reflected waves are in-phase when the reflection phase falls between ±90 deg. This is also the bandwidth of the EBG structure.

The method of simulating reflection phase can also be employed as a quick way to compare different types of EBG structures. Here, a UC-PBG structure is modeled in HFSS. For a fair comparison, the UC-PBG is designed using the same substrates, as well as the same slot width (0.2 mm) and strip width (0.3 mm). The result in Figure 2-24 shows that UC-PBG structure has a period of 12.6 mm when it is working around 2.45 GHz. Since the proposed EBG structure has a period of 8.9 mm, and taking into account that it has cascade LC circuits in each unit cell, the overall size reduction is 64.7%.

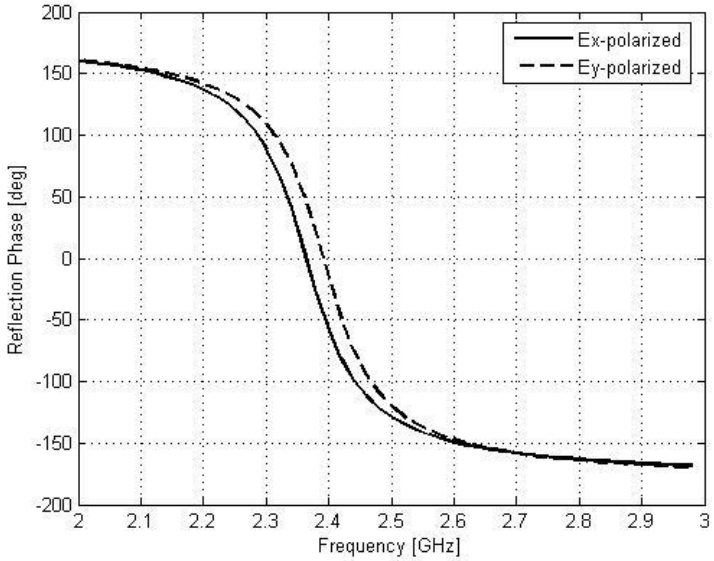

Figure 2-23 Reflection phase of the proposed EBG structure: W_h= 0.15mm, W_v= 0.15mm, W_t= 1, W_f= 0.3, L_c= 2.4mm, h_1= 1.27mm, h_2=3.175 mm, d= 0.2mm.

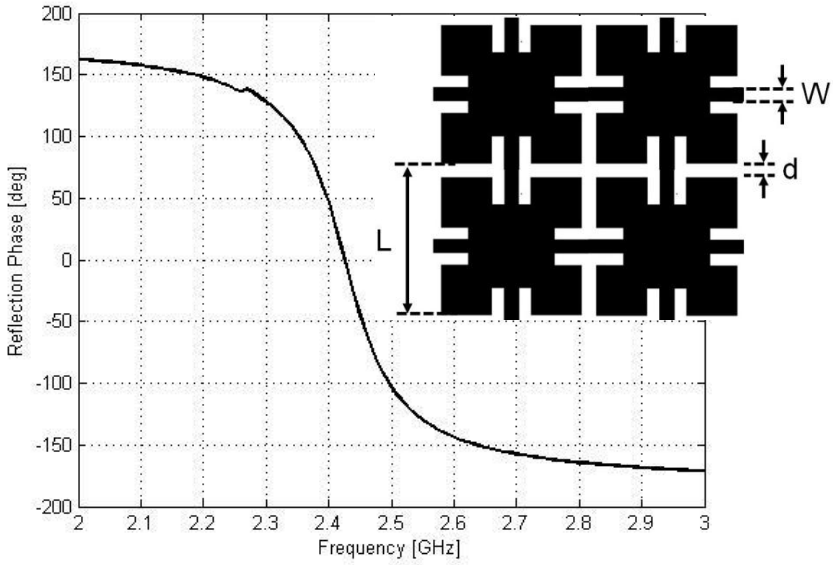

Figure 2-24 Reflection phase of a UC-PBG structure: W= 0.3mm, d= 0.2mm, L=12.6mm.

2.3.5 Parameter Study

Parameter study of the compact EBG structure is conducted by using the reflection phase model introduced in the last section. Results of several key parameters are shown from Figure 2-25 to Figure 2-29. For each parameter, two different polarization directions are simulated.

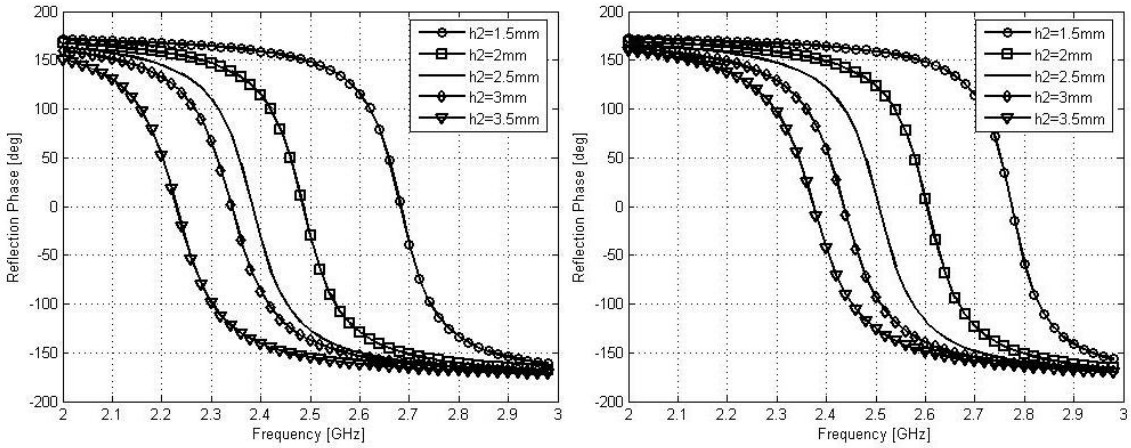

(a) (b)

Figure 2-25 Reflection phase for different values of h_2. (a) E_x-polarized and (b) E_y-polarized incident wave.

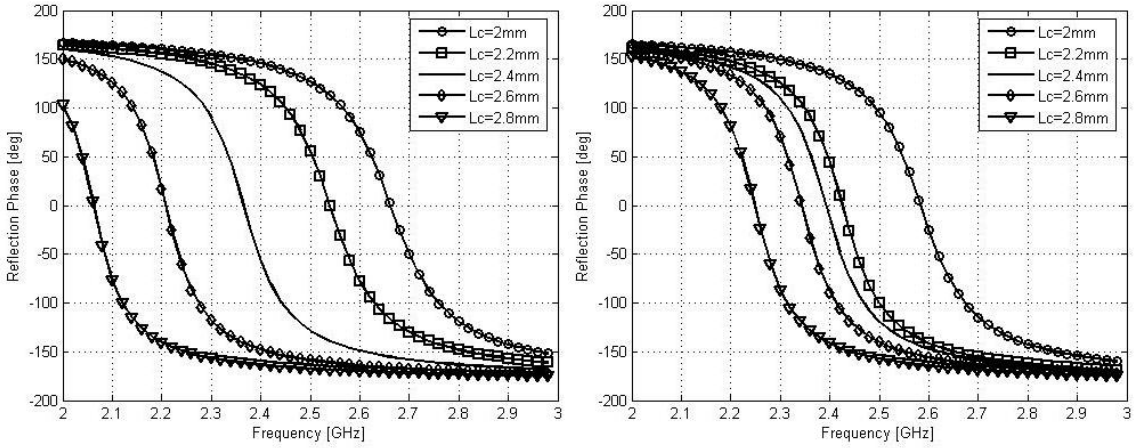

(a) (b)

Figure 2-26 Reflection phase for different values of L_c. (a) E_x-polarized and (b) E_y-polarized incident wave.

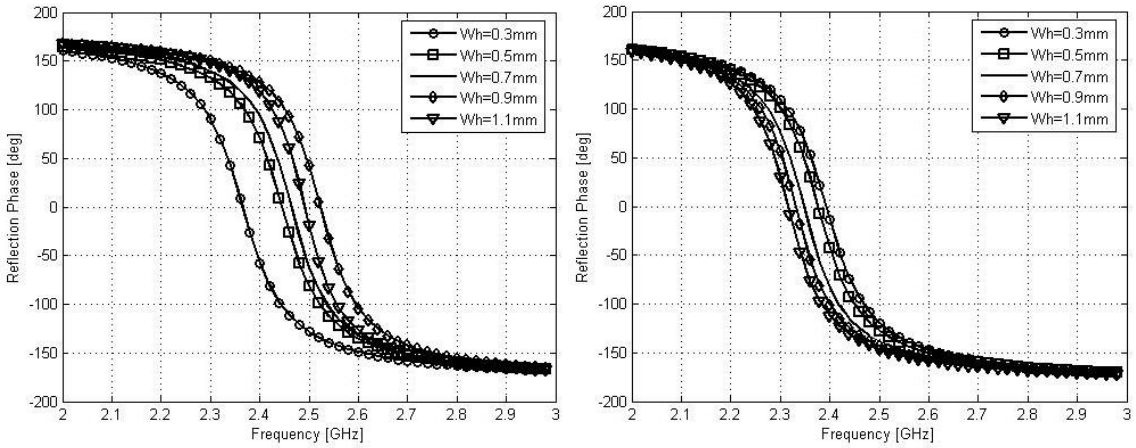

(a) (b)

Figure 2-27 Reflection phase for different values of W_h. (a) E_x-polarized and (b) E_y-polarized incident wave.

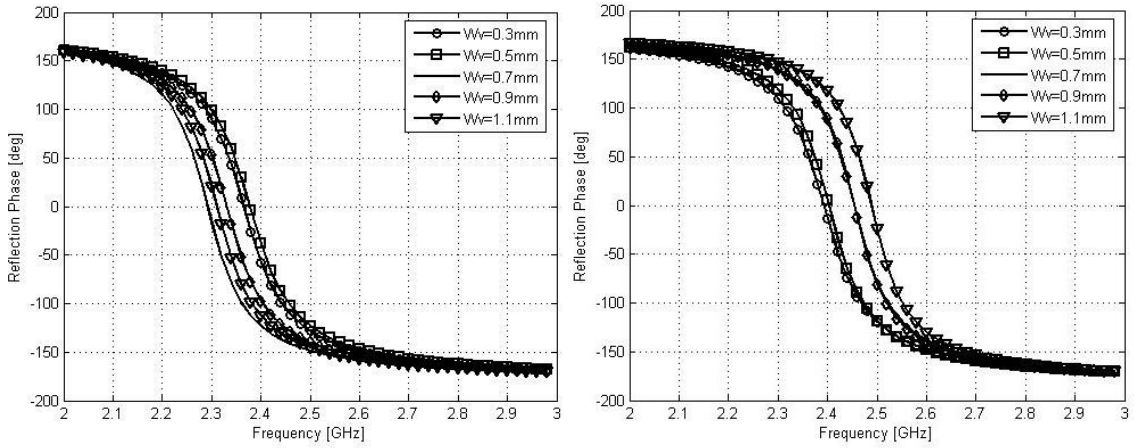

(a) (b)

Figure 2-28 Reflection phase for different values of W_v. (a) E_x-polarized and (b) E_y-polarized incident wave.

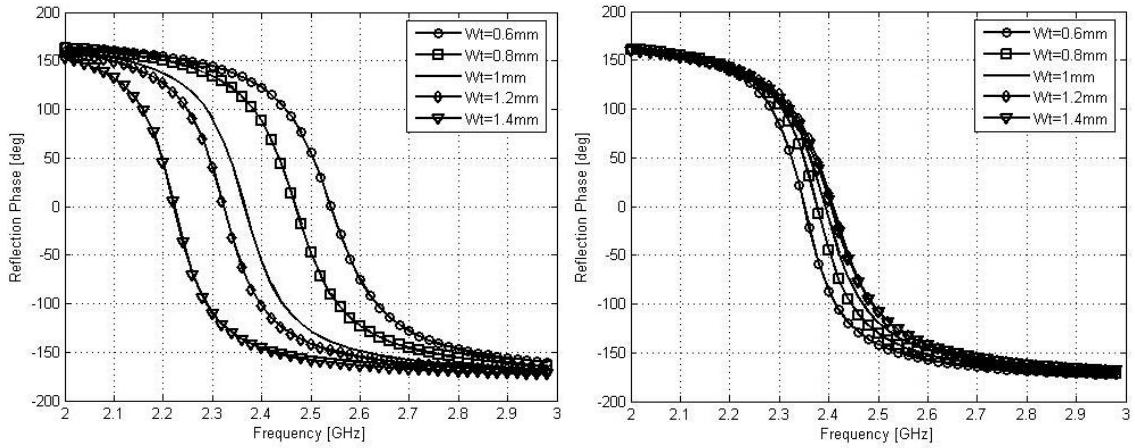

(a) (b)

Figure 2-29 Reflection phase for different values of W_t. (a) E_x-polarized and (b) E_y-polarized incident wave.

From Figure 2-25, we can see the bottom substrate height (h_2) significantly influences the resonance and bandwidth. Using thicker substrate leads to lower resonant frequency as well as larger bandwidth (the frequency range between ±90 deg). Another factor that effectively affects the performance is the finger-length of the inter-digital capacitor (L_c), which determines value of the effective capacitance. As L_c increases, both resonant frequency and bandwidth of the surface structure decreases, as a direct result of (2.3.2) and (2.3.3).

2.3.6 Dispersion Diagram

The frequency band-gap of an EBG structure can also be seen from its dispersion diagram, as we discussed in Section 2.1. In this section, HFSS eigenmode solver is applied to simulate the dispersion diagram.

Wave propagation characteristics in a 2-D periodic structure can be demonstrated by employing Brillouin Zone in its unit cell. This method has been fully illustrated in [46], [47]. The basic idea is to analyze the performance of the structure along the main sides of an irreducible Brillouin Zone instead of analyzing all possible propagation directions. For the proposed EBG structure, the Brillouin Zone in its unit cell is shown in Figure 5-14. k_x and k_y are wave vectors in two orthogonal directions. Positions of the four critical points [48] Γ, X, M, Y are (0,0), $(\pi/d, 0)$, $(\pi/d, \pi/d)$ and $(0,\ \pi/d)$, respectively.

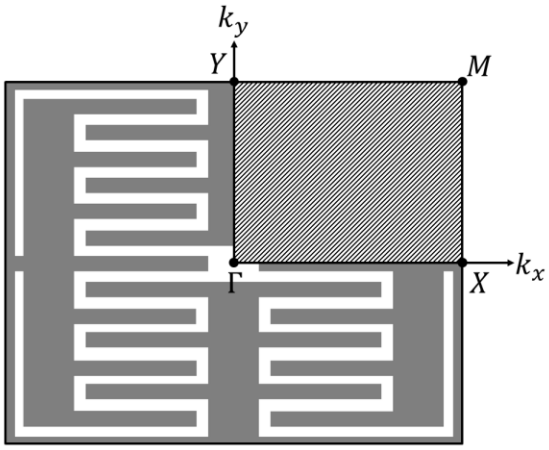

Figure 2-30 Brillouin Zone in a unit cell of the compact high-impedance surface.

The analysis starts from Γ point and first goes through the $\Gamma - X$ line by varying k_x from 0 to π/d. Then, the analysis carries on along the $X - M$ line. This can be done by holding k_x at π/d and varying k_y from 0 to π/d. Next, the surface property is examined along the $M - Y$ line by keeping k_y at π/d and changing k_x from π/d to 0. Finally, it returns to Γ point through the $Y - \Gamma$ line by varying k_x from π/d to 0.

A unit cell model of the proposed EBG structure is built in HFSS using the method introduced in Section 2.3.3. A perfect matched layer (PML) boundary is defined on top of

the model to imitate an infinite free space above the surface, as shown in Figure 2-31. Here, we define the pair of master-slave boundaries normal to the x-axis as B1 and the other pair of master-slave boundaries as B2 for convenience.

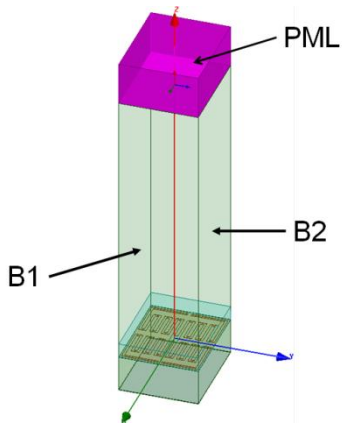

Figure 2-31 Unit cell model with PML on top boundary.

The model is simulated by HFSS eigenmode solver. Variables for the parametric analysis are the phase differences between each opposing pair of master-slave boundaries. By calculating solutions for every phase difference, a plot of phase difference against solution frequencies tracing one side of the Brillouin Zone is obtained. Since the phase difference is proportional to the wave number for a certain solution frequency, this plot can be also treated as dispersion diagram of the EBG structure.

For solution frequencies in the $\Gamma - X$ line, the phase difference of B2 is held constant at zero and phase difference of B1 is varied from 0 deg to 180 deg. For solution frequencies along the $X - M$ line, the phase difference of B1 is held constant at 180 deg while the phase difference of B2 is increased from 0 deg to 180 deg. For the $M - Y$ line, the phase difference of B2 is held constant at 180 degr and phase between of B1 is varied from 180 deg to 0 deg. Finally, for the $Y - \Gamma$ line, the phase between of B1 is held zero while the phase of B2 decreases from 180 deg to 0 deg.

Result of dispersion curves are shown in Figure 2-32. The horizontal axis represents phase differences along the Brillouin Zone boundaries, which is analogous to wave numbers plotted in a true dispersion diagram. The maximum value of the first dispersion mode determines the lower limit of the band-gap, which is about 2.45 GHz. The intersection of

the second mode dispersion curve and the light line at around is the upper limit of the band-gap, which is around 2.55 GHz. Examining the area between the lower and upper limits, a band-gap of approximately 100 MHz is observed (the narrow grey strip in Figure 2-32). These eigenmode solutions closely match reflection phase results in Section 2.3.4.

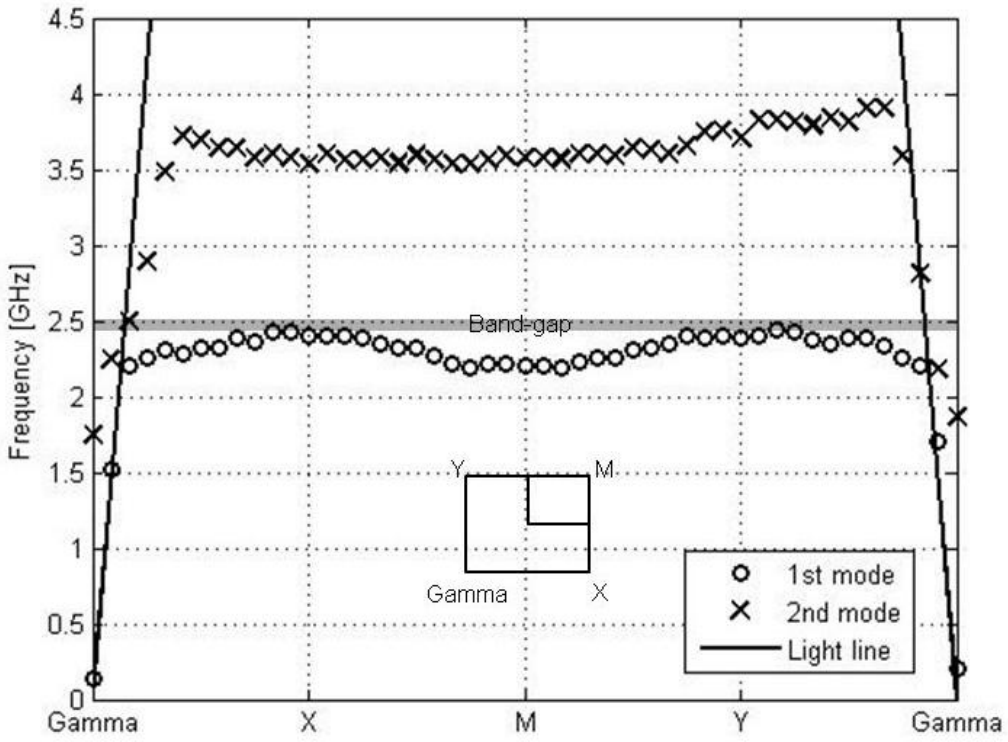

Figure 2-32 Dispersion Diagram of the proposed EBG structure: W_h= 0.15mm, W_v= 0.15mm, W_t= 1, W_f= 0.3, L_c= 2.4mm, h_1= 1.27mm, h_2=3.175 mm, d= 0.2mm.

2.3.7 Finite-element Model

To further demonstrate band-gap performance of the proposed EBG structure, two finite-element models integrated with 50 Ohm microstrip lines are built, as shown in Figure 2-33 and Figure 2-34. The two microstrip lines are arranged in different directions with respect to the EBG structure. Compared with the monopole measurement in [1], the suspended microstrip line has a stronger coupling with the measured periodic surface. Thus, the influence of other parasitic propagation modes is reduced and the band-gap performance is exhibited more obviously in the S-parameter plot [34].

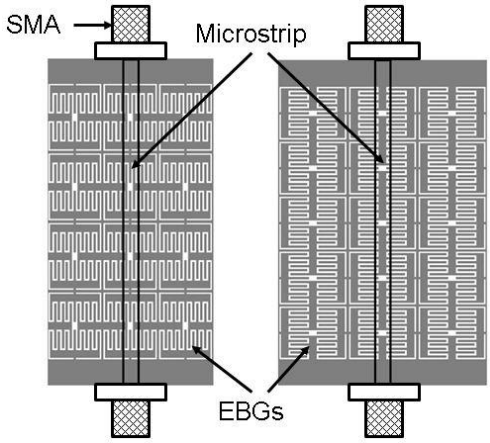

Figure 2-33 Top view of finite-element models integrated with microstrips (a) horizontally and (b) vertically: W_h= 0.15mm, W_v= 0.15mm, W_t= 1, W_f= 0.3, L_c= 2.4mm, h_1= 1.27mm, h_2=3.175 mm, d= 0.2mm.

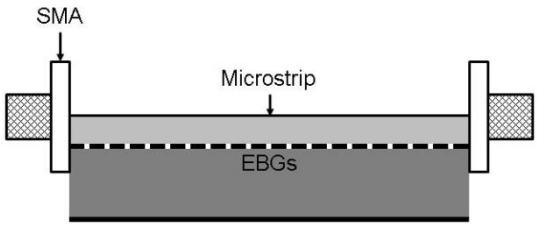

Figure 2-34 Cross section of finite-element models integrated with microstrops: W_h= 0.15mm, W_v= 0.15mm, W_t= 1, W_f= 0.3, L_c= 2.4mm, h_1= 1.27mm, h_2=3.175 mm, d= 0.2mm.

The simulation results of S-parameters are shown in Figure 2-35. As we can see, a distinctive band-gap ranges approximately from 2.35 GHz to 2.55 GHz is observed for both directions of propagation, where the transmission coefficient (S_{21}) is lower than -15 dB.

However, ripples are found due to the multipath reflection effect. The return loss (S_{11}) is close to 0 dB in the band-gap, indicating little radiation loss.

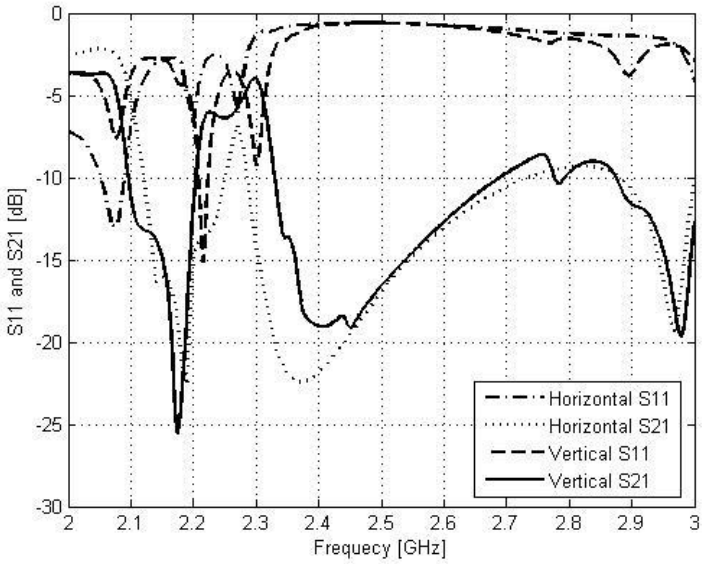

Figure 2-35 S-parameters of finite-element models integrated with microstrips in different directions: W_h= 0.15mm, W_v= 0.15mm, W_t= 1, W_f= 0.3, L_c= 2.4mm, h_1= 1.27mm, h_2=3.175 mm, d= 0.2mm.

Chapter 3

EBG Antenna

High-impedance EBG structures have been widely employed as ground planes to improve antenna performance [49], [50], [51], [52], [53], [54], [55]. Compared to a flat metal ground plane, an EBG plane prevents surface wave, leading to less backward radiation of an antenna. Thus, power wasted in the undesired direction is reduced, as shown in Figure 3-1.

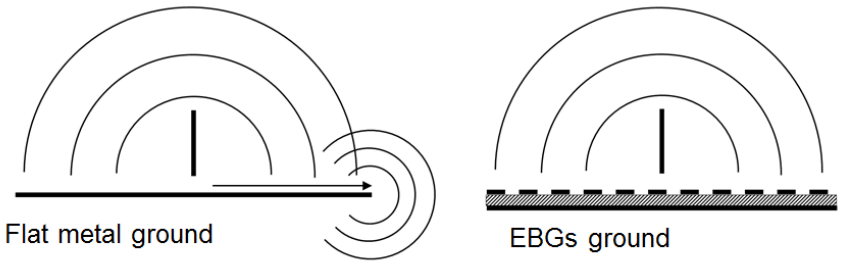

Figure 3-1 Antennas on a flat metal ground and an EBG ground.

Another important property of the EBG structure is its zero degree reflection phase, which allows antennas to produce in-phase image currents. This can be applied to various antenna designs.

This chapter starts with analyzing radiation fields of current elements on a ground plane with arbitrary reflection phase. The effect of reflection phase on total radiated power is discussed. A patch antenna and a two-element antenna array are integrated with the structure proposed. Simulations results of these antennas in HFSS are obtained. The goal is to miniaturize ground plane size without increasing back radiation of the antenna system.

3.1 Current Elements on Ground Plane

The analysis of a radiation problem, where an infinitesimal current source locates above an infinite lossless surface, can be simplified by employing image theory. The phase of the image current depends on the surface properties.

3.1.1 Parallel Current Element

In Figure 3-2, a current source is placed parallel to an infinite lossless surface with a normal distance d. Radiation field of the current source in free space is given by expressions below, where $r \gg \lambda$.

$$E_\theta = \eta \frac{jIl}{2\lambda r} e^{-jkr} \sin\theta \tag{3.1.1}$$

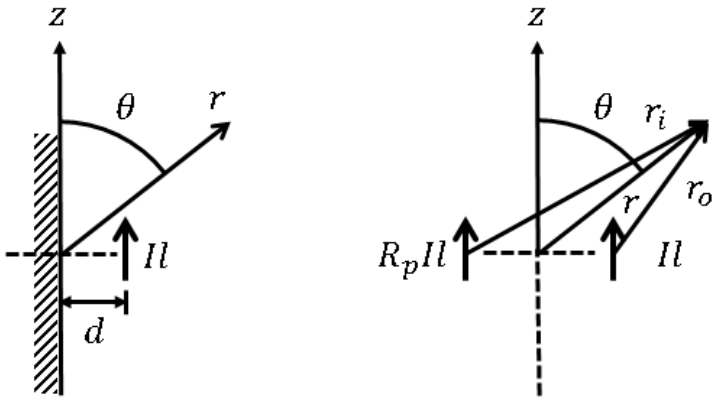

Figure 3-2 A current source is in parallel with an infinite surface: original problem and simplified model.

Assuming the surface produces an image current which is relate to the original source through a complex surface reflection coefficient denoted by R_p. Then, the total radiation field is the superposition of the two elements, ignoring presence of the surface.

$$E_{total} = \eta \frac{jIl}{2\lambda} \left(\frac{e^{-jkr_0}}{r_o} + R_p \frac{e^{-jkr_i}}{r_i} \right) \sin\theta \tag{6.1.2}$$

r_0 and r_i can be easily obtained as

$$r_0 = r - d\cos\theta \tag{3.1.3a}$$

$$r_i = r + d\cos\theta \tag{3.1.3b}$$

In the far field where $r \gg d$, inserting (3.1.3) into (3.1.2) yields

$$E_{total} = \eta \frac{jIle^{-jkr}}{2\lambda r} \sin\theta \left[e^{jkd\cos\theta} + R_p e^{-jkd\cos\theta}\right] \tag{3.1.4}$$

Since $H_\phi = E_\theta/\eta$, the total magnetic field in the far region is calculated as

$$H_{total} = \frac{jIle^{-jkr}}{2\lambda r} \sin\theta \left[e^{jkd\cos\theta} + R_p e^{-jkd\cos\theta}\right] \tag{3.1.5}$$

The total radiated power by the system is then determined as follow

$$P = \iint_{hemisphere} E_{total} H^*_{total}\, ds = \pi\eta \int_0^\pi |H_{total}|^2 r^2 \sin\theta\, d\theta \tag{3.1.6}$$

Substituting from (3.1.5) and integrating, we have

$$P = 2\pi\eta \left|\frac{Il}{\lambda}\right|^2 \left(\frac{1}{3} - Re\{R_p\}\frac{\cos 2kd}{(2kd)^2} + Re\{R_p\}\frac{\sin 2kd}{(2kd)^3}\right) \tag{3.1.7}$$

In practical application, especially for microstrip antennas, it is properly to assume $\lambda \gg d$, which means $kd \to 0$. Thus, (3.1.7) can be further simplified as

$$P \approx \frac{2\pi\eta}{3} \left|\frac{Il}{\lambda}\right|^2 \left(1 + Re\{R_p\}\right) \tag{3.1.8}$$

If we assume that $R_p = e^{j\delta_p}$, then for a PEC surface, δ_p has the value of π. The total power radiated by the system is almost zero. This result reflects the fact a parallel current source placed sufficiently close to an infinite PEC surface can hardly radiates to the space. On the other hand, for a surface that has a zero reflection phase ($\delta_p = 0$), or PMC, the total

radiated power to the right half space is doubled compared to the same current source radiating in free space.

3.1.2 Vertical Current Element

Similarly, the total radiated power of a current source vertically placed above an infinite surface is obtained using the simplified model shown in Figure 3-3.

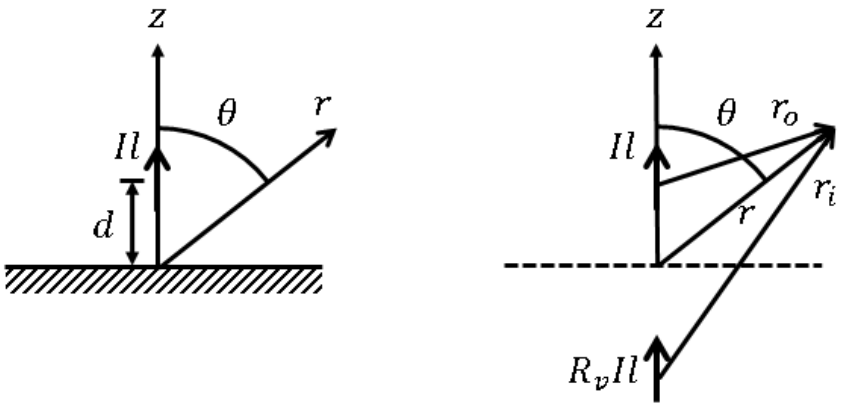

Figure 3-3 A current source is placed vertically to an infinite surface: original problem and simplified model.

In this case, we again assume that $R_v = e^{j\delta_v}$. The result is similar to that in (3.1.8), except that for this situation, δ_v has the value of π when the surface is a PMC surface, while it equals to 0 when the surface is a PEC surface. Thus, a vertical current source can hardly radiate on a PMC surface, but is a good radiator on a PEC surface.

3.2 Patch Antenna

Patch antenna is one of the most common antenna configurations in communication systems due to their advantages of low-profile, simple fabrication and integration with accompanying electronics. However, conventional patch antennas suffer from the effects of surface waves which cause backward direction radiation, especially when thick or high dielectric constant substrates are used [56]. Although larger ground planes can compensate this problem, it is still an issue when compact structures are required. To overcome this disadvantage, the compact EBG structure in Section 2.3 is integrated with a patch antenna working at 2.45 GHz as the ground plane.

3.2.1 Design

Top view of the designed EBG structure patch antenna is shown in Figure 3-4(a), grey areas represent metal material and circles represent the 50 Ohm coax feeding from the bottom. On the bottom substrate (left figure), none unit cells are textured at the center area (underneath the patch). The patch is etched on the top substrate and is centered with respect to the ground plane (right figure). Dimension details are listed in Table 3-1. The substrate heights and dielectric constants are identical to the dimensions in Table 2-1.

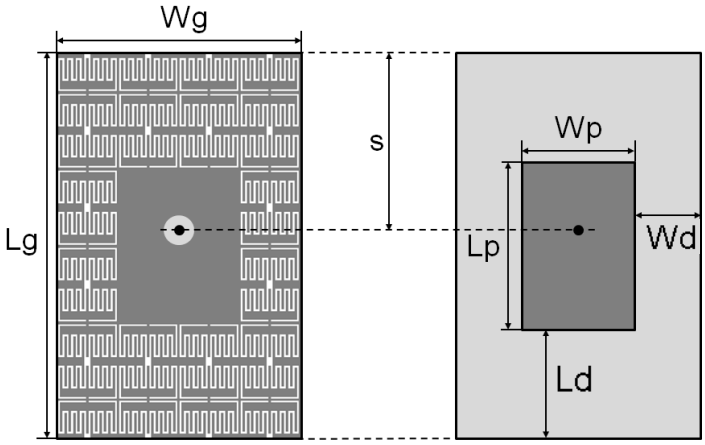

(a)

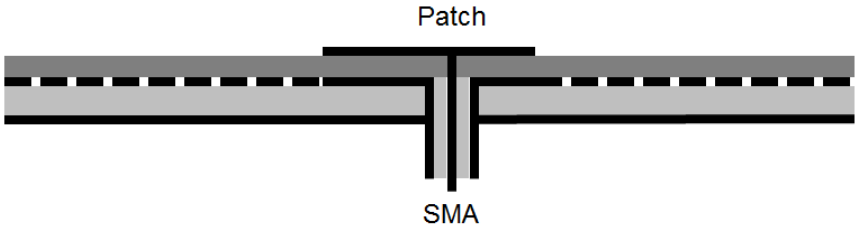

(b)

Figure 3-4 A patch antenna integrated with EBG ground: (a) top view of bottom substrate (left) and top substrate (right), (b) cross section.

Table 3-1 Dimensions of the patch antenna

Parameter	Dimensions [mm]	Parameter	Dimensions [mm]
L_g	44.8	W_g	28.3
L_p	18.8	W_p	13
L_d	13	W_d	7.65
s	19.3		

3.2.2 Result

For comparison, an identical patch antenna using ordinary ground is modeled as a reference. In both cases, the input impedances are matched to 50 Ohm for a fair comparison. Figure 3-5 plots simulated return loss of the two configurations – ordinary patch and EBG patch.

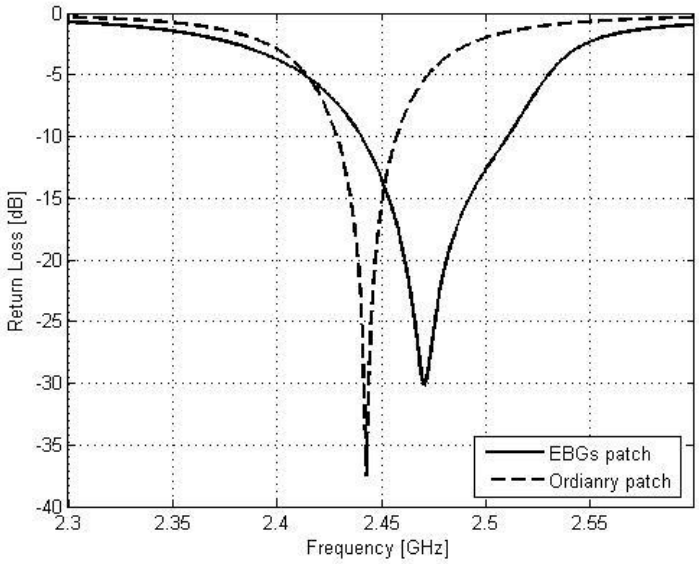

Figure 3-5 Simulated S_{11} of patch antennas with different types of ground: W_h= 0.15mm, W_v= 0.15mm, W_t= 1, W_f= 0.3, L_c= 2.4mm, h_1= 1.27mm, h_2=3.175 mm, d= 0.2mm.

In Figure 3-5, minimum peak of S_{11} of the EBG antenna is at 2.47 GHz. The EBG ground antenna has a bandwidth of 3.04%, where the return loss is less than -10 dB. This is much larger than bandwidth of the reference antenna, which is only 1.23%. Also, the presence of EBG structure tends to raise the resonance. This is due to the coupling between the patch and surrounding unit cells reduces the effective cavity volume. Note that the band-gap of the ground must be larger than the antenna bandwidth so that it can cover the operational band of the antenna. Figure 3-6 plots the E-plane and H-plane normalized radiation patterns for both the ordinary and EBG patch antennas. The measured frequency is at 2.44 GHz for the ordinary patch and 2.47 GHz for the EBG patch, where both antennas have the lowest return loss.

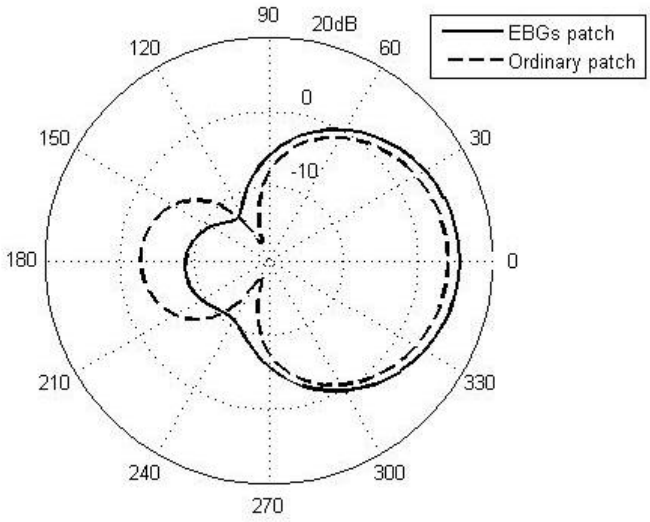

(a)

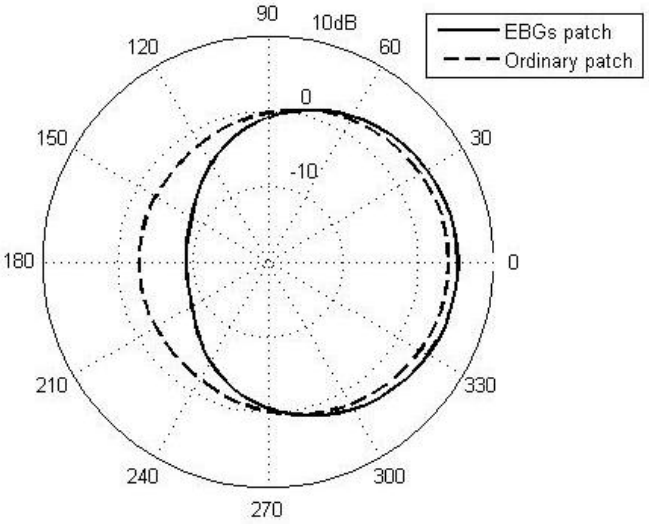

(b)

Figure 3-6 (a) E-plane and (b) H-plane radiation patterns of patch antennas with different types of ground: W_h= 0.15mm, W_v= 0.15mm, W_t= 1, W_f= 0.3, L_c= 2.4mm, h_1= 1.27mm, h_2=3.175 mm, d= 0.2mm.

In the forward direction, nearly 1.3 dB enhancement of the radiation pattern can be seen. A more obvious influence of the EBG ground on radiation pattern is observed in the backward direction. The gain of EBG antenna at 180 deg is 7 dB less than that of the ordinary one, which means little backward radiation. The results demonstrate a significantly suppression of surface waves. Overall, the EBG ground reshapes the radiation pattern, providing a more focused radiation beam in the forward direction.

3.3 Antenna Array

A patch antenna array can provide much higher gain than a single patch with little extra cost. However, due to existence of surface waves and space waves, strong mutual coupling usually exists between radiating elements [57].This coupling degrades the steering of radiation beam, causing blind angles. Since EBG structures have been proved to suppress surface waves, it is natural to integrated them into patch antenna arrays to reduce mutual coupling in the system.

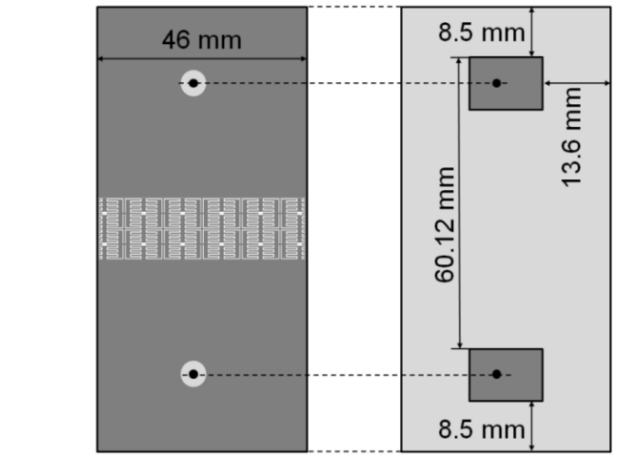

(a)

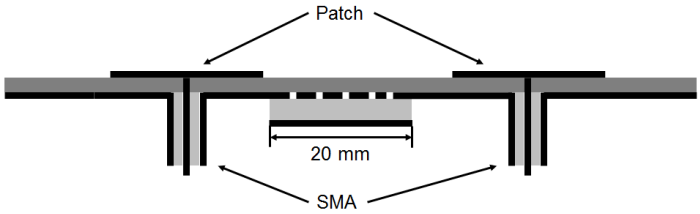

(b)

Figure 3-7 A patch array integrated with EBG ground: (a) top view of bottom substrate (left) and top substrate (right), (b) cross section.

3.3.2 Result

The simulated mutual coupling (S_{21}) and return loss (S_{11}) with and without EBG structure are shown in Figure 3-8. As revealed in the figure, the antenna array shows stronger mutual coupling of -21 dB on an ordinary ground. The special structure inserted effectively reduces the mutual coupling between the patch elements. As a consequence, S_{21} of the array with EBG structure is only -27 dB at resonance. An approximately 6 dB reduction of mutual coupling is achieved. Thus, it can be concluded that the EBG structure can be utilized for mutual coupling reduction in antenna arrays.

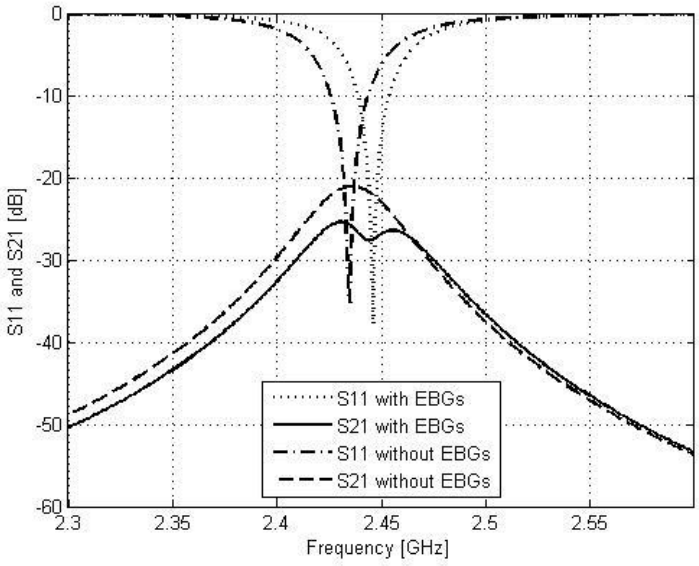

Figure 3-8 S-parameters of patch antenna arrays with and without EBG structure: W_h= 0.15mm, W_v= 0.15mm, W_t= 1, W_f= 0.3, L_c= 2.4mm, h_1= 1.27mm, h_2=3.175 mm, d= 0.2mm.

Chapter 4

Conclusion and Future Work

4.1 Summary

In this dissertation, a novel EBG structure has been introduced. Compared to previous designs, it has a compact configuration and easy to be integrated with other RF/microwave components. Simulations have shown the effectiveness of the compact EBG structure in surface wave suppression and in-phase reflection. Further, a patch antenna mounted on the EBG ground plane shown a great improvement in radiation performance with respect to the same patch etched on a conventional substrate. The radiation patterns show a more focused beam with over 1.2 dB improvement of maximum gain and a significant 7 dB reduction of back radiation. This will lead to the possibility of integrating antennas on high dielectric constant substrates without losing performance, as well as reducing undesired coupling with nearby systems. For an antenna array, a 6 dB reduction in mutual coupling is observed by integrating EBG structure between radiating elements, which might provide a practical solution for eliminating blind angles.

4.2 Future Work: EBG Antenna for Body Area Network (BAN) Devices

Since the EBG antennas have characteristics of compactness and low back radiation, it is particularly applicable for portable devices near human body, where the interaction between the antenna and the user can have a significant impact on antenna performance. The EBG ground plane redirects the antenna radiation that would otherwise be absorbed into the user, recovering it as useful power in the opposite direction, which leads to higher radiation efficiency, longer battery life, and smaller size in BAN devices.

To study antenna performance near human body, we should first understand the electromagnetic properties of body tissues, which vary significantly with frequency and tissue types. Electromagnetic properties of human body tissues at RF/microwave frequencies have been examined in several studies [58], [59], [60], [61], [62]. A recent

comprehensive research is described in [63], where excised animal tissues and human autopsy materials were measured from 10 Hz to 20GHz. An analytical model for the permittivity of different materials was developed based on a 4-Cole-Cole expression [63],

$$\varepsilon(\omega) = \varepsilon_\infty + \sum_{m=1}^{4} \frac{\Delta\varepsilon_m}{1 + (j\omega\tau_m)^{(1-\alpha_m)}} + \frac{\sigma_j}{j\omega\varepsilon_0} \tag{4.2.1}$$

Here, ε_∞ is the material permittivity at terahertz frequency. ε_0 is the material permittivity in free space. σ_j is the material conductivity. ε_m, τ_m and α_m are material parameters for each dispersion region. Based on (4.2.1), relative permittivity, loss tangent, and penetration depth for different human body tissues were reported in [63]. Particularly, we are interested in tissue properties at 2.45 GHz. For muscle tissue, its electromagnetic properties at 2.45 GHz are listed in Table 4-1.

Table 4-1 Electromagnetic properties of human muscle at 2.45GHz

Material	Conductivity [S/m]	Relative Permittivity	Loss Tangent	Penetration Depth [m]
Muscle	1.773	52.668	0.24205	0.021886

Using data in Table 4-1, the interaction between the antenna and human body is modeled by a $16 \times 16 \times 1\ cm^3$ muscle material in EM simulator (HFSS), as shown in Figure 4-1. The size of the muscle material is relatively small due to the memory limit of the computer. Although this is only a coarse model for human body, a significant reduction of radiation into muscle model, as well as a great improvement in radiation efficiency can still be observed in Figure 4-2 and Figure 4-3.

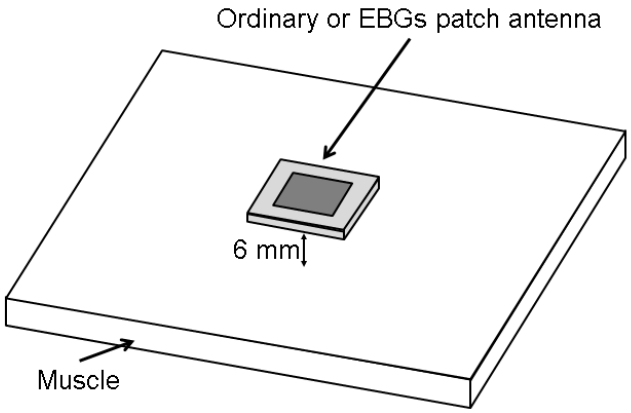

Figure 4-1 Patch antennas with or without EBG structure on human muscle.

Further accurate verification of the EBG antenna performance near human body need to be conducted by using physical body phantoms [64], where sensitive absorption rate (SAR) for both ordinary patch antenna and EBG patch antenna cases can be measured.

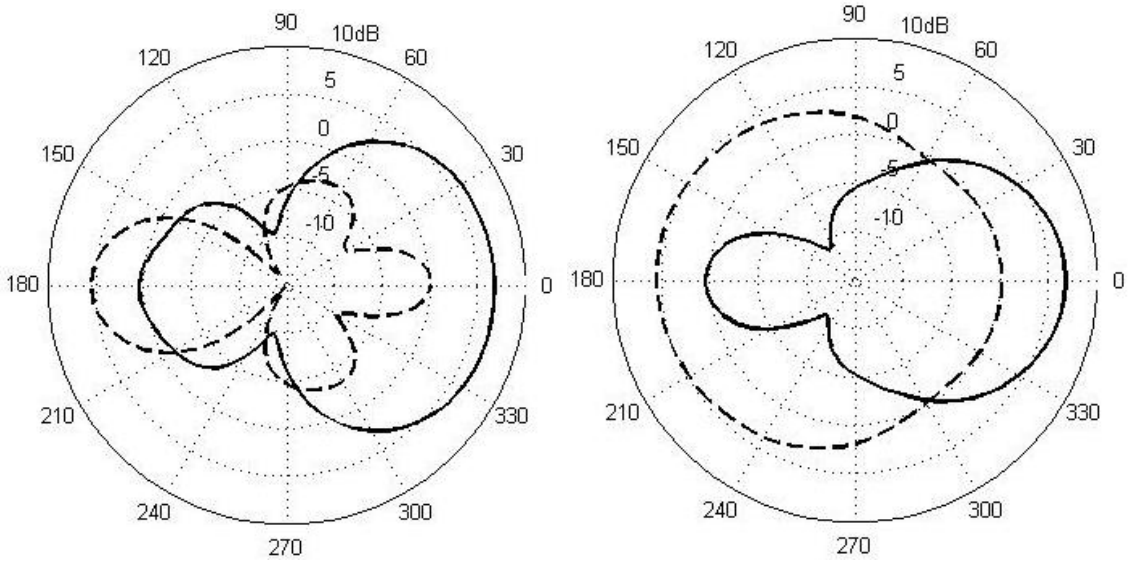

(a) (b)

Figure 4-2 Radiation Pattern of ordinary and EBG patch antennas near muscle tissue: (a) E-plane ('-' EBG patch, '--' ordinary patch) and (b) H-plane ('-' EBG patch, '--' ordinary patch): W_h= 0.15mm, W_v= 0.15mm, W_t= 1, W_f= 0.3, L_c= 2.4mm, h_1= 1.27mm, h_2=3.175 mm, d= 0.2mm.

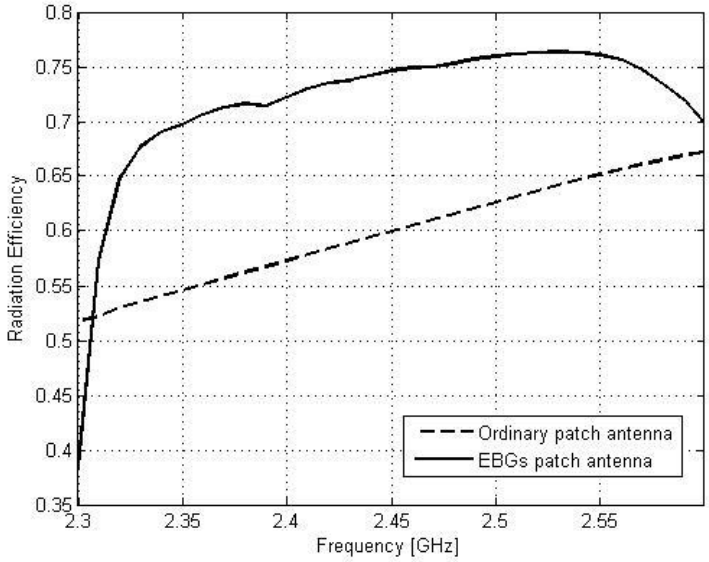

Figure 4-3 Radiation efficiency of ordinary patch antenna and EBG patch antenna near muscle tissue: W_h= 0.15mm, W_v= 0.15mm, W_t= 1, W_f= 0.3, L_c= 2.4mm, h_1= 1.27mm, h_2=3.175 mm, d= 0.2mm.

Appendix A

Surface Waves

Surface waves are defined as waves bounded to an interface between two different dielectric media [65]. These waves propagate parallel to the interface and diminish exponentially away from the interface. In this part, wave propagation of transverse magnetic TM waves and transverse electric TE waves are illustrated on different interfaces. Firstly, surface waves are analyzed on a dielectric interface. We find that for both TM and TE waves, propagation only exist on materials with a non-positive dielectric constant, such as metal [66]. Secondly, surface wave behaviour is illustrated on a metal-dielectric interface. The result shows that on an ordinary flat metal-dielectric interface, surface waves can propagate at the speed of light and they are simply surface currents [1]. At last, surface wave properties on a general impedance surface is determined. It turns out that TM waves can only propagate when the surface impedance has a positive reactance, while TE waves can only occur when the surface impedance has a negative reactance.

Dielectric Interfaces

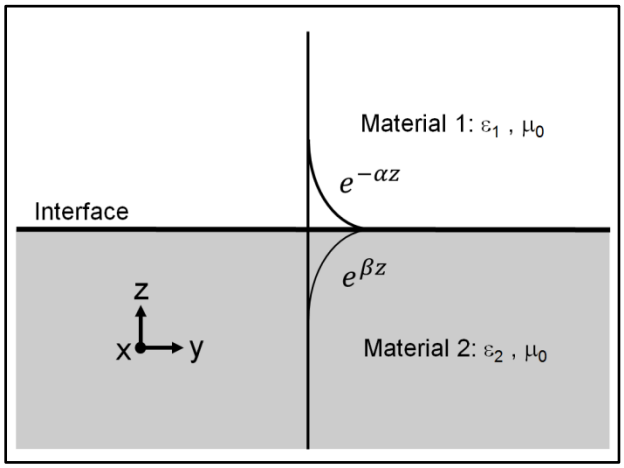

Figure A-1 A surface wave on a dielectric interface.

For a general dielectric interface, we consider material 1 occupies the upper half space having a dielectric constant ε_1 and material 2 takes the lower half space with a dielectric constant ε_2 . The interface is in the XY plane, as shown in Figure A-1. Assuming that the surface wave on the interface attenuates in the $+Z$ direction with an attenuation constant α. In the $-Z$ direction, the surface wave attenuates with an attenuation constant β.

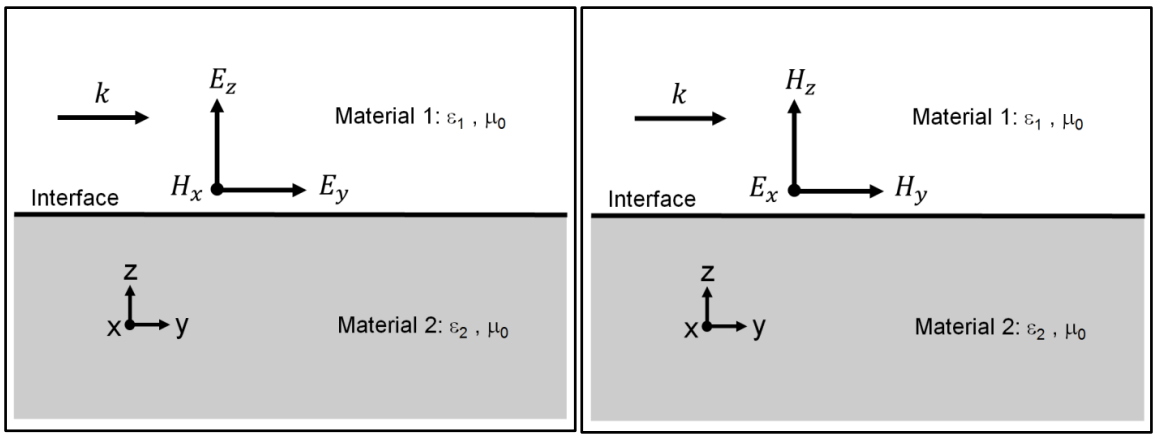

(a) (b)

Figure A-2 (a) TM and (b) TE waves on dielectric interfaces.

For a TM surface wave in material 1, as shown in Figure A-2(a), the electromagnetic field is given in (A.1), where the time harmonic factor $e^{j\omega t}$ is omitted and A, B, C, D are constants.

$$E_x = 0 \tag{A.1a}$$

$$E_y = Ae^{-jky-\alpha z} \tag{A.1b}$$

$$E_z = Be^{-jky-\alpha z} \tag{A.1c}$$

$$H_y = 0 \tag{A.1d}$$

$$H_z = 0 \tag{A.1e}$$

With (A.1), H_x can be derived from the Ampere's law.

$$\nabla \times \vec{H} = j\omega\varepsilon\vec{E}$$

$$H_x = -\frac{j\omega\varepsilon}{\alpha} Ae^{-jky-\alpha z} \tag{A.2}$$

The electromagnetic field in material 2 has the same form of (A.1) and (A.2) but with different attenuation constant,

$$E_x = 0 \tag{A.3a}$$

$$E_y = Ce^{-jky+\beta z} \tag{A.3b}$$

$$E_z = De^{-jky+\beta z} \tag{A.3c}$$

$$H_y = 0 \tag{A.3d}$$

$$H_z = 0 \tag{A.3e}$$

$$H_x = j\omega\varepsilon/\beta \; Ae^{-jky+\beta z} \tag{A.3f}$$

Bearing in mind that the electric fields and electric displacements at the interface must satisfy boundary conditions,

$$Ae^{-jky-\alpha 0^+} = Ce^{-jky+\beta 0^-}$$

$$\varepsilon_1 B e^{-jky-\alpha 0^+} = \varepsilon_2 \, D e^{-jky+\beta 0^-}$$

That is,

$$A = C \tag{A.4a}$$

$$\varepsilon_1 B = \varepsilon_2 \, D \tag{A.4b}$$

Recalling Maxwell's equations,

$$\nabla \times \vec{H} = j\omega\varepsilon\vec{E} \tag{A.5}$$

$$\nabla \times \vec{E} = -j\omega\mu\vec{H} \tag{A.6}$$

Combining the two equations (A.5) and (A.6), we yield the relationship below.

$$\nabla \times \nabla \times \vec{E} = \omega^2 \mu_0 \varepsilon \vec{E} \tag{A.7}$$

Noticing that for TM surface waves, the electric field in X direction is zero, then (A.7) can be expanded as,

$$\left(\frac{\partial^2 E_z}{\partial z \partial y} - \frac{\partial^2 E_y}{\partial z^2}\right)\hat{u}_y + \left(\frac{\partial^2 E_y}{\partial z \partial y} - \frac{\partial^2 E_z}{\partial y^2}\right)\hat{u}_z = \omega^2 \mu_0 \varepsilon \left(E_y \hat{u}_y + E_z \hat{u}_z\right) \tag{A.8}$$

Inserting (A.1), (A.3) and (A.4) into (A.8), we can obtain equations for the fields on both sides of the interface. Here ε_{r1} and ε_{r2} are relative dielectric constant of material 1 and material 2, respectively.

$$jk\alpha B - \alpha^2 A = \omega^2 \mu_0 \varepsilon_0 \varepsilon_{r1} A \tag{A.9a}$$

$$jk\alpha A + k^2 B = \omega^2 \mu_0 \varepsilon_0 \varepsilon_{r1} B \tag{A.9b}$$

$$-\beta^2 A - jk\beta \frac{\varepsilon_1}{\varepsilon_2} B = \omega^2 \mu_0 \varepsilon_0 \varepsilon_{r2} A \tag{A.9c}$$

$$-jk\beta A + k^2 \frac{\varepsilon_1}{\varepsilon_2} B = \omega^2 \mu_0 \varepsilon_0 \varepsilon_{r1} B \tag{A.9d}$$

Finally, the wave vector k, the attenuation constant α and β are given by solving (A.9).

$$k = \omega\sqrt{\mu_0\varepsilon_0}\sqrt{\frac{\varepsilon_{r1}\varepsilon_{r2}}{\varepsilon_{r1}+\varepsilon_{r2}}} \tag{A.10a}$$

$$\alpha = \omega\sqrt{\mu_0\varepsilon_0}\sqrt{\frac{-{\varepsilon_{r1}}^2}{\varepsilon_{r1}+\varepsilon_{r2}}} \tag{A.10b}$$

$$\beta = \omega\sqrt{\mu_0\varepsilon_0}\sqrt{\frac{-{\varepsilon_{r2}}^2}{\varepsilon_{r1}+\varepsilon_{r2}}} \tag{A.10c}$$

With (A.10), surface waves on a general interface between two dissimilar materials are fully described. If both ε_{r1} and ε_{r2} are positive, then α and β will be imaginary, which means that the waves will go through the interface instead of attenuating away, so TM wave do not exist on interface between dielectrics. However, if the material on one side is dielectric while the material on the other side is metal with large imaginary permittivity [68], α and β will be complex numbers. Thus, the solution describes a surface wave bounded to the interface.

We can analyze TE surface waves by applying principle of duality [69]. The result is same with (A.10).

$$\vec{E} \rightarrow \vec{H}$$

$$\varepsilon \rightarrow \mu$$

Metal-dielectric Interfaces

Metal-dielectric interfaces often occur in practical problems, especially for PCB technology. In this part, surface waves on a metal-dielectric interface will be discussed, as shown in Figure A-3.

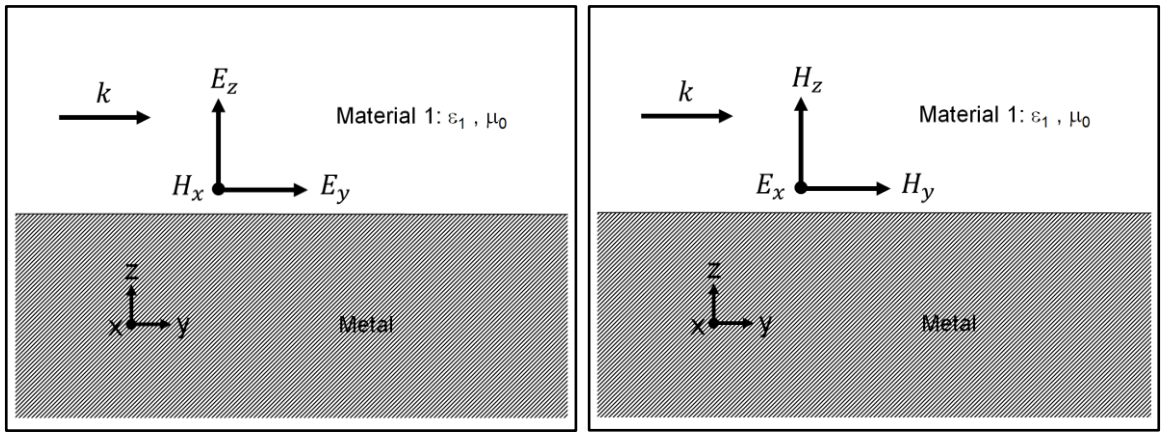

(a) (b)

Figure A-3 (a) TM and (b) TE waves on metal-dielectric interfaces.

At radio frequencies, the effective relative dielectric constant of a metal material is basically a large imaginary number [68], which can be expressed as,

$$\varepsilon_r(\omega) \approx \frac{j\sigma}{\omega\varepsilon_0} \tag{A.11}$$

Where σ is the metal conductivity and $\sigma/\omega\varepsilon_0 \gg 1$. For example, the conductivity of copper equals to 5.96×10^7 S/m. With radio frequencies ranging from 3 kHz to 300 GHz, the imaginary part of effective relative dielectric constant varies from 2.24×10^7 to 2.24×10^{16}, which is much larger than its real part 1.

Conclusions from (A.10) can be directly applied here by substituting ε_{r2} with ε_r in (A.11). The result shows dispersion relation of surface waves on a metal-dielectric interface, which is

$$k \approx \frac{\omega}{c_0}\sqrt{\varepsilon_{r1}}$$

or

$$k = \frac{\omega}{c_1} \tag{A.12}$$

Here c_0 is the velocity of light in vacuum, c_1 is the velocity of light in material 1. (A.12) gives the fact that surface waves on a metal-dielectric interface travels nearly at the speed of light.

Impedance surfaces

The surface waves can also be analyzed on impedance surfaces. Figure A-4 shows an impedance surface in the XY plane with surface impedance Z_s, the material above the surface has a dielectric constant ε_1. A surface wave is bounded to the impedance surface, propagating in the $+Y$ direction with propagation constant k and attenuating in the $+Z$ direction with attenuation constant α.

For the electric field above the impedance surface, we can apply Helmholtz equation.

$$\nabla^2\vec{E} + k^2\vec{E} = 0 \tag{A.13}$$

Substituting $\vec{E}$ in (A.13) with expressions in (A.1), we obtain the relationship between the wave number k and the attenuation constant α.

$$\alpha^2 + \omega^2\mu_0\varepsilon_1 - k^2 = 0$$

or

$$k = \sqrt{\alpha^2 + \omega^2\mu_0\varepsilon_1} \tag{A.14}$$

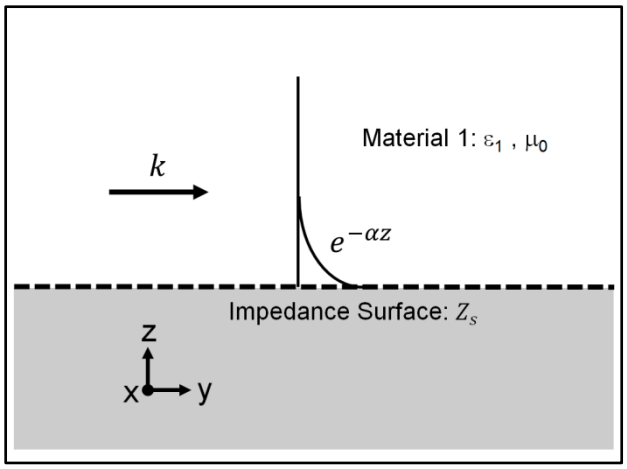

Figure A-4 A surface wave on a dielectric interface.

Figure A-5(a) shows a TM surface wave propagating on a general impedance surface. Again we express it as in (A.1) and (A.2),

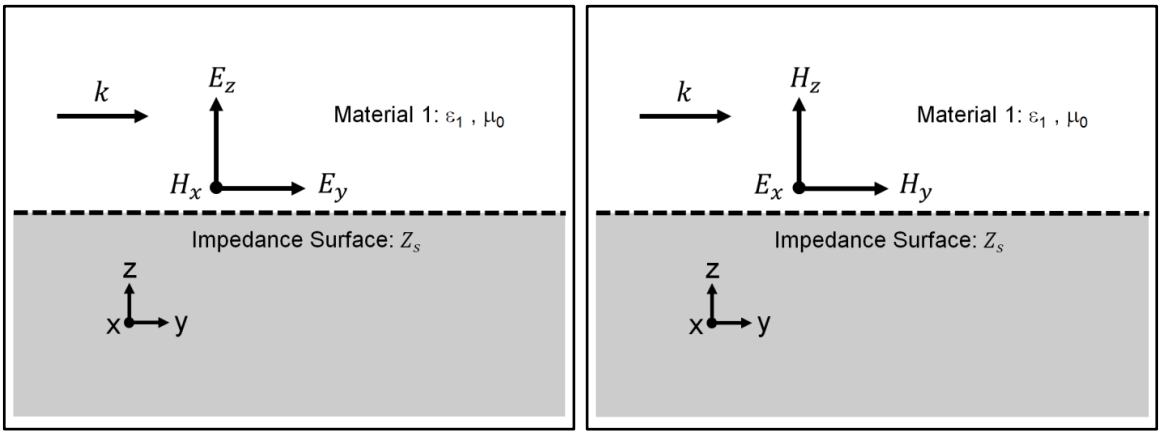

(a) (b)

Figure A-5 (a)TM and (b)TE surface waves on impedance surfaces.

$$E_y = Ae^{-jky-\alpha z} \tag{A.15a}$$

$$H_x = -\frac{j\omega\varepsilon}{\alpha} Ae^{-jky-\alpha z} \tag{A.15b}$$

Defining surface impedance Z_s in terms of E_y and H_x as,

$$Z_s = \frac{E_y}{H_x} \tag{A.16}$$

Substituting E_y and H_x in (A.16) with expressions in (A.15) gives the surface impedance for TM surface waves.

$$Z_{sTM} = \frac{j\alpha}{\omega\varepsilon} \tag{A.17}$$

Combining (A.14) and (A.17) leads to

$$k_{TM} = \frac{\omega}{c_1}\sqrt{1 - \frac{{Z_{sTM}}^2}{{\eta_1}^2}} \tag{A.18}$$

(A.18) is the dispersion relation for a TM surface wave on impedance surface, where η_1 is the intrinsic impedance of material 1.

Using the geometry shown in Figure A-5(b), the surface impedance for TE surface waves can be determined. In the same manner, we first express electromagnetic field for TE waves upon the impedance surface.

$$E_x = \frac{j\omega\mu}{\alpha} A' e^{-jky-\alpha z} \tag{A.19a}$$

$$H_y = A' e^{-jky-\alpha z} \tag{A.19b}$$

Surface impedance seen by TE waves is given as,

$$Z_s = -\frac{E_x}{H_y} \tag{A.20}$$

Then we have,

$$Z_{sTE} = -\frac{j\omega\mu}{\alpha} \tag{A.21}$$

Again we combine (A.14) and (A.21) as in the TM case and have,

$$k_{TE} = \frac{\omega}{c_1}\sqrt{1 - \frac{{\eta_1}^2}{{Z_{sTE}}^2}} \tag{A.22}$$

(A.22) gives the dispersion relation of a TE surface wave on an impedance surface.

(A.17) and (A.21) show us that TM waves can only exist on a surface with inductive surface impedance. While for TE waves, capacitive surface impedance is required for the wave propagation.

Bibliography

[1] D. Sievenpiper, L. Zhang, R. F. J. Broas, N. G. Alexopolous, E. Yablonovitch,, "High-Impedance Electromagnetic Surfaces with a Forbidden Frequency Band," *IEEE Transactions on Microwave Theory and Techniques,* vol. 47, no. 11, pp. 2059-2074, 1999.

[2] Y. J. Lee, J. Yeo, R. Mittra, W. S. Park, "Application of Electromagnetic Bandgap (EBG) Superstrates With Controllable Defects for a Class of Patch Antennas as Spatial Angular Filters," *IEEE Transactions on Antennas and Propagation,* vol. 53, no. 1, pp. 224-235, 2005.

[3] S. G. Mao, M. Y. Chen, "Propagation Characteristics of Finite-Width Conductor-Backed Coplanar Waveguides with Periodic Electromagnetic Bandgap Cells," *IEEE Transactions on Microwave Theory and Techniques,* vol. 50, no. 11, pp. 2691-2703, 2002.

[4] F. Yang, Y. Rahmat-Samii, "Reflection Phase Characterizations of the EBG Ground Plane for Low Profile Wire Antenna Applications," *IEEE Transactions on Antennas and Propagation,* vol. 51, no. 10, pp. 677-682, 2003.

[5] D. H. Schaubert, D. M. Pozar, A. Adrian, "Effect of microstrip antenna substrate thickness and permittivity," *IEEE Transactions on Antennas and Propagation,* vol. 37, no. 6, pp. 677-682, 1989.

[6] J. H. Lu, K. L. Wong, "Slot-loaded meandered rectangular microstrip antenna with compact dual frequency operation," *Electronic Letters,* vol. 34, pp. 1048-1050, 1998.

[7] R. Porath, "Theory of miniaturized shorting-post microstrip antennas," *IEEE Transactions on Antennas and Propagation,* vol. 48, no. 1, pp. 41-47, 2000.

[8] J. L. Volakis, C. C. Chen, K. Fujimoto, Small Antennas: Miniaturization Techniques & Application, New York: McGraw-Hill, 2010.

[9] J.M. Bell, M.F. Iskander, "A Low-Profile Archimedean Spiral Antenna Using an EBG Ground Plane," *IEEE antennas and wireless propagation letters,* vol. 3, pp. 223-226, 2004.

[10] F. Yang, K. Ma, Y. Qian, T. Itoh, "A Uniplanar Compact Photonic-Bandgap (UC-PBG) Structure And Its Applications For Microwave Circuits," *Ieee Transactions on Microwave Theory,* vol. 47, no. 8, pp. 1509-1514, 1999.

[11] D. Swanson, W. Hoefer, Microwave Circuit Modeling Using Electromagnetic Field Simulation, Boston: Artech House, 2003.

[12] G. Shaker, "Electromagnetic Band Gap Structures:Design and Application in Antenna Systems," *MASc. dissertation, Department of Electrical and Computer Engineering, University of Waterloo, Waterloo, ON,* 2006.

[13] F. Yang, Y. Rahmat-Samii, "A low-profile circularly polarized curl antenna over an electromagnetic bandgap (EBG) surface," *Microwave and Optical Technology Letters,* vol. 31, no. 4, pp. 264-267, 2001.

[14] Z. Li, Y. Rahmat-Samii, "PBG, PMC and PEC ground planes: A case study of dipole antennas," in *IEEE Antennas and Propagation Society International Symposium*, 2000.

[15] T. H. Liu, W. X. Zhang, M. Zhang, K. F. Tsang, "Low profile spiral antenna with PBG substrate," *Electronics Letters,* vol. 36, p. 779–780, 2000.

[16] S. Bashir, M. Hosseini, R. M. Edwards, M. I. Khattak, L. Ma, "Bicep Mounted Low Profile Wearable Antenna Based on A Non-Uniform EBG Ground Plane – Flexible

EBG Inverted-L (FEBGIL)," in *Loughborough antennas and propagation conference*, Loughborough, 2008.

[17] N. Chahat, M. Zhadobov, R. Sauleau, K. Mahdjoubi, "Improvement of the On-Body Performance of a Dual-Band Textile Antenna Using an EBG structure," in *Loughborough antennas and propagation conference*, Loughborough, 2010.

[18] J. H. S. D. Sievenpiper, "Textured Surface Having High Electromagnetic Impedance in Multiple Frequency Bands". United States Patent US 6,483,481 B1, 19 November 2002.

[19] R. Li, G. DeJean, M. M. Tentzeris, J. Papapolymerou, J. Laskar, "Radiation-Pattern Improvement of Patch Antennas on a Large-Size Substrate Using a Compact Soft-Surface Structure and Its Realization on LTCC Multilayer Technology," *IEEE Transactions on antennas and propagation*, vol. 53, no. 1, pp. 200-208, 2005.

[20] R. Diaz, V. Sanchez, E. Caswell, A. Miller, "Magnetic Loading of Artificial Magnetic Conductors for Bandwidth Enhancement," 2003.

[21] Aminian, F. Yang, Y. Rahmat-Samii, "In-phase Reflection and EM Wave Suppression Characteristics of Electromagnetic Band Gap Ground Planes," IEEE Antennas and Propagation Society International Symposium," 2003.

[22] Aminian, Y. Rahmat-Samii, "Bandwidth Determination for Soft and Hard Ground Planes: A Unified Approach in Visible and Surface Wave Regions," in *IEEE Antennas and Propagation Society International Symposium*, 2004.

[23] F. Bilotti, L. Vegni, "Radiating Features of Capacitive and Inductive Surfaces," *Microwave and Optical Technology Letters*, vol. 39, no. 2, pp. 117-121, 2003.

[24] H.Y.D. Yang, N.G. Alexopoulos, E. Yablonovitch, "Photonic Band-Gap Materials For High-Gain Printed Circuit Antennas," *IEEE Transactions On Antennas And Propagation,* vol. 45, no. 1, pp. 185-187, 1997.

[25] F. Caminita, S. Costanzo, G. Di Massa, G. Guarnieri, S. Maci, G. Mauriello, And I. Venneri, "Reduction Of Patch Antenna Coupling By Using A Compact EBG Formed By Shorted Strips With Interlocked Branch-Stubs," *IEEE Antennas And Wireless Propagation Letters,* vol. 8, pp. 811-814, 2009.

[26] Liang Chen, Chun Wang, Qi Zhang And Xiangsong Yang, "A Novel Wide-Band Cascaded EBG Structure With Chip Capacitors Loading," in *IEEE International Microwave, Antenna, Propagation, and EMC Technologies For Wireless Communications Symposium,* 2011.

[27] D. M. Pozar, Microwave Engineering, Reading, MA: Addison-Wesley, 1990.

[28] H. Raether, Surface Plasmons on Smooth and Rough Surfaces and on Gratings, Berlin, Germany: Springer-Verlag, 1988.

[29] E. Rajo-Iglesias, L. Inclan-Sanchez, J.-L.Vazquez-Roy, E. Garcia-Munoz, "Size Reduction Of Mushroom-Type EBG Surfaces By Using Edge-Located Vias," *IEEE Microwave and Wireless Components Letters,* vol. 17, no. 9, pp. 670-672, 2007.

[30] L. Inclan-Sanchez, J.-L.Vazquez-Roy, E. Rajo-Iglesias, E. Garcia-Munoz, "Compact EBG Surface Based on Capacitively Loaded Loop Resonators With Grounded Vias," in *The Second European Antenna And Propagation Conference*, Edinburgh, UK, 2007.

[31] M. Sagawa, K. Takahashi, M. Makimoto, " Miniaturized Hairpin Resonator Filters And Their Application To Receiver Front-End MICs," *IEEE Transactions on Microwave Theory And Techniques,* vol. 37, no. 12, pp. 1991-1997, 1989.

[32] R. Coccioli, F. R. Yang, K. Ma And T. Itoh, "Aperture Coupled Patch Antenna On UC-PBG Substrate," *IEEE Transactions on Microwave Theory And Techniques,* vol. 47, no. 11, pp. 2123-2130, 1999.

[33] Y. Qian, T. Itoh, "Microwave Applications Of Photonic Band-Gap (PBG) Structures," in *Asia Pacific Microwave Conference*, Singapore, 1999.

[34] L. Yang, M. Fan, F. Chen, J. She, Z. Feng, " A Novel Compact Electromagnetic-Bandgap (EBG) Structure And Its Applications For Microwave Circuits," *IEEE Transactions On Microwave Theory And Techniques,* vol. 53, no. 1, pp. 183-190, 2005.

[35] D. Gary, "Inter-Digital Capacitors And Their Application To Lumped-Element Microwave Integrated Circuits," *IEEE Transactions on Microwave Theory and Techniques,* vol. 18, no. 12, p. 1028–1033, 1970.

[36] S. Rogers, W. Mckinzie, G. Mendolia, "AMCs Comprised Of Interdigital Capacitor FSS Layers Enable Lower Cost Applications," in *IEEE Antennas And Propagation Society International Symposium*, 2003.

[37] Y. Fu, N. Yuan, G. Zhang, "Compact High-Impedance Surfaces Incorporated With Interdigital Structure," *Electronics Letters,* vol. 40, no. 5, pp. 310-311, 2004.

[38] Arriola, G. Sasiain, J.I. Sancho, J. Parrón, J. Gemio, R. Villarino, "Compact High Impedance Surface Based On Interdigital Capacitors," in *Proceedings Of The Fourth European Conference On Antennas And Propagation*, Barcelona, Spain, 2010.

[39] I.J. Bahl, P. Bhartia, Microwave Solid-State Design, New York: John Wiley & Sons, 1988.

[40] K. J. Vinoy, K. A. Jose, V. K. Varadan, V. V. Varadan, "Hilbert Curve Fractal Antenna: A Small Resonant Antenna For VHF/UHF Applications," *Microwave and Optical Technology Letters,* vol. 29, no. 4, p. 215–219, 2001.

[41] S. R. Best, "A Comparison Of The Performance Properties Of The Hilbert Curve Fractal And Meander Line Monopole Antennas," *Microwave and Optical Technology Letters,* vol. 35, no. 4, p. 258–262, 2002.

[42] J. Zhu, A. Hoorfar, N. Engheta, "Bandwidth, Cross Polarization, And Feed-Point Characteristics Of Matched Hilbert Antennas," *IEEE Antennas and Wireless Propagation Letters,* vol. 2, no. 1, p. 2–5, 2003.

[43] E. A. Parker, A. N. A. El Sheikh, "Convoluted Array Elements And Reduced Size Unit Cells For Frequency-Selective Surfaces," *IEE Proceedings H: Microwaves, Antennas, and Propagation,* vol. 138, no. 1, p. 19–22, 1991.

[44] J. Mcvay, N. Engheta, A. Hoorfar, "High Impedance Metamaterial Surfaces Using Hilbert-Curve Inclusions," *IEEE Microwave And Wireless Components Letters,* vol. 14, no. 3, pp. 130-132, 2004.

[45] R. Remski, "Analysis of Photonic Bandgap Surfaces Using Ansoft HFSS," *Microwave Journal,* 2000.

[46] A. Grbic, G. Eleftheriades, "Periodic analysis of a 2-D negative refractive index transmission line structure," *IEEE Transactions on Antennas and Propagation,* vol. 51, no. 10, pp. 2604-2611, 2003.

[47] G. Eleftheriades, K. G. Balmain, Negative Refraction Metamaterials: Fundamental Principles and Applications, New York: Wiley-IEEE Press, 2005.

[48] Wikipedia, [Online]. Available: http://en.wikipedia.org/wiki/Brillouin_zone.

[49] S.G. Mao, C.M. Chen, D.C. Chang, "Modeling of Slow-Wave EBG Structure for Printed-Bowtie Antenna Array," *IEEE antennas and wireless propagation letters,* vol. 1, no. 1, pp. 124-127, 2002.

[50] G.K. Palikaras, A.P. Feresidis, J.C. Vardaxogolu, "Cylindrical Electromagnetic Bandgap Structures for Directive Base Station Antennas," *IEEE antennas and wireless propagation letters,* vol. 3, no. 1, pp. 87-89, 2004.

[51] Z. Iluz, R. Shavit, R. Bauer, "Microstrip Antenna Phased Array With Electromagnetic Bandgap Substrate," *IEEE Transactions on Antenna and Propagation,* vol. 52, no. 6, pp. pp1446-1453, 2004.

[52] H. Nakano, Y. Asano, J. Yamauchi, "A Wire Inverted-F Antenna on a Finite-Sized EBG Material," in *IEEE International Workshop on Antenna Technology: Small Antennas and Novel Metamaterials*, 2005.

[53] R. Chantalat, C. Menudier, M. Troubat, E. Arnaud, T. Monediere, M Thevenot, B Jecko, P. Dumon, "Enhanced Two Level EBG Antenna for A High F/D Multibeam Reflector Antenna in Ka Band: Design and Characterization," in *The Second European Conference on Antennas and Propagation*, 2007.

[54] S. Zhu, R. Langley, "Dual-Band Wearable Textile Antenna on an EBG Substrate," *IEEE Transactions on Antenna and Propagation,* vol. 57, no. 4, pp. 926-935, 2009.

[55] S. Kwak, D.U. Sim, J. H. Kwon, "Design of Optimized Multilayer PIFA With the EBG Structure for SAR Reduction in Mobile Applications," *IEEE transactions on electromagnetic compatibility,* vol. 53, no. 2, pp. 325-331, 2011.

[56] C. A. Balanis, Antenna Theory: Analysis and Design, 3rd ed., New York: Wiley, 2005.

[57] F. Yang, Y. Rahmat-Samii, "Microstrip Antennas Integrated With Electromagnetic Band-Gap (EBG) Strectures: A low Mutual Coupling Design for Array Application," *IEEE Transactions on Antennas and Propagation,* vol. 51, no. 10, pp. 2936-2946 , 2003.

[58] C. H. Durney, H. Massoudi, M. F. Iskander, Radiofrequency Radiation Dosimetry Handbook, Brooks Air Force Base-USAFSAM-TR-85-73, 1986.

[59] L. A. Geddes, L. E. Barker, "The Specific Resistance of Biological Material-A Compendium of Data for the Biomedical Engineer and Physiologist," *Medical and Biological Engineering,* vol. 5, pp. 271-293, 1967.

[60] M. A. Stuchly, S. S. Stuchly, "Dielectric Properties of Biological Substances-Tabulated," *Journal of Microwave Power,* vol. 15, no. 1, pp. 19-26, 1980.

[61] K. R. Froster, H. P. Schwan, "Dielectric Properties of Tissues and Biological Materials: A Critical Review," *Critical Review in Biomedical Engineering,* vol. 17, no. 1, pp. 25-104, 1989.

[62] F. A. Duke, Physical Properties of Tissue: A Comprehensive Reference Book, New York: Academic Press, 1990.

[63] C. Gabriel, "Compilation of the Dielectric Properties of Body Tissues at RF and Microwave Frequencies," Brooks Air Force Technical Report, AL/OE-TR-1996-0037, 1996.

[64] P. S. Hall, Y. Hao, Antennas and Propagation for Body-Centric Wireless

Communications, Boston: Artech House, 2006.

[65] R. Collin, Field Theory of Guided Waves, 2nd ed., New York: IEEE Press, 1991.

[66] D. Sievenpiper, "High-impedance electromagnetic surfaces," *Ph.D. Dissertation, Department of Electrical Engineering, UCLA, Los Angeles, CA*, 1999.

[67] D. S. E. Yablonovitch, "Circuit and method for eliminating surface currents on metals". United States Patent US 6,262,495 B1, 17 July 2001.

[68] G. Burns, Solid State Physics, Orlando: Academic Press, 1985.

[69] Roger F. Harrington, Time-harmonic Electromagnetic Fields, Now York: IEEE press, 2001.